Ge dots and nanostructures grown epitaxially on Si

2006 J. Phys.: Condens. Matter 18 R139

(http://iopscience.iop.org/0953-8984/18/8/R01)

INSTITUTE OF PHYSICS PUBLISHING JOURNAL OF PHYSICS: CONDENSED MATTER

J. Phys.: Condens. Matter **18** (2006) R139–R174 doi:10.1088/0953-8984/18/8/R01

TOPICAL REVIEW

Ge dots and nanostructures grown epitaxially on Si

J-M Baribeau[1], X Wu[1], N L Rowell[2] and D J Lockwood[1]

[1] Institute for Microstructural Sciences, National Research Council Canada, Ottawa, ON, K1A 0R6, Canada
[2] Institute for National Measurements Standards, National Research Council Canada, Ottawa, ON, K1A 0R6, Canada

Received 15 June 2005
Published 10 February 2006
Online at stacks.iop.org/JPhysCM/18/R139

Abstract

We review recent progress in the growth and characterization of $Si_{1-x}Ge_x$ islands and Ge dots on (001) Si. We discuss the evolution of the island morphology with $Si_{1-x}Ge_x$ coverage, and the effect of growth parameters or post-growth annealing on the shape of islands and dots. We outline some of the structural, vibrational, and optical properties of $Si_{1-x}Ge_x$ islands and review recent advances in the determination of their composition and strain distribution. In particular, we present an analytical electron transmission microscopy study of the Ge spatial distribution in Ge dots and $Si/Si_{1-x}Ge_x$ island superlattices grown by molecular beam epitaxy and ultra-high vacuum chemical vapour deposition. We describe the use of undulated $Si_{1-x}Ge_x$ island superlattices for infrared detection at telecommunication wavelengths. Finally, we discuss various approaches currently being investigated to engineer $Si_{1-x}Ge_x$ quantum dots and, in particular, control their size, density, and spatial distribution. As examples, we show how C pre-deposition on Si(001) can influence nucleation and growth of Ge islands and how low temperature Si homo-epitaxy can lead to a particular surface cusp morphology that may promote dot nucleation.

(Some figures in this article are in colour only in the electronic version)

Contents

1. Introduction and historical perspective

The growth of semiconductor three-dimensional (3D) islands and quantum dots and the study of their physical properties have been a very active area of research in the last 15 years. These novel nanostructures offer interesting prospects for the development of new electronic, photonic, or optoelectronic devices. Accurate control of the size, shape, and position of the dots is, however, crucial for the exploitation of these nanostructures in quantum devices such as qbits and single-photon emitters or, alternatively, for their use as nano-templates for surface functionalization. $Si_{1-x}Ge_x$ on Si is one of the best studied systems exhibiting self-organized nanostructures in semiconductor heteroepitaxy. When deposited on (001) Si, Ge and $Si_{1-x}Ge_x$ alloys can undergo a transition from planar two-dimensional (2D) growth to a 3D island structure [1–5]. This phenomenon occurs when the development of this 3D morphology is energetically favourable to the generation of structural defects such as misfit dislocations for the accommodation of the strain [6, 7].

Considerable work has been done on the growth and characterization of $Si_{1-x}Ge_x$ islands and Ge dots and important results have been discussed in several reviews [8–12]. The rapid expansion of research activity in the growth, characterization and exploitation of Ge nanostructures can be appreciated by a (non-comprehensive) sampling of related papers published in major research journals, as depicted in figure 1. The first reports of Ge island structures on (001) Si can be traced back to the late 1980s. After an initial period focused on the synthesis of dots and their morphological evolution, the research emphasis has moved toward the study of their optical properties and the possible exploitation of $Si_{1-x}Ge_x$-based nanostructures as photon detectors. The mapping of the Ge concentration and strain profile of Ge nanostructures has been the subject of a number of investigations in the past five years. Finally, considerable efforts are currently devoted to dot engineering, i.e., devising methods to control the size, position, and density of dots.

Here we briefly outline progress in the growth and characterization of $Si_{1-x}Ge_x$ three-dimensional heterostructures on (001) Si. More specifically, we discuss two classes of systems, namely $Si_{1-x}Ge_x$ island superlattices obtained by depositing alternating Ge-rich alloy layers and pure Si layers, and Ge dots obtained by depositing thin layers of pure Ge on a (001) Si substrate. We discuss the evolution of the island morphology with $Si_{1-x}Ge_x$ coverage, we look at the effect of the growth parameters or post-growth treatments on the shape of the islands and we review recent developments in the determination of the composition and strain distribution of individual $Si_{1-x}Ge_x$ islands. We also discuss the properties of $Si/Si_{1-x}Ge_x$ island superlattices and present a comparative study of structures grown by molecular beam epitaxy (MBE) and ultra-high vacuum chemical vapour deposition (UHV-CVD). The optical properties of dots and islands are reviewed, as well as applications in their infrared photodetection. Finally, we describe various approaches that are currently being investigated to engineer $Si_{1-x}Ge_x$ islands and Ge dots.

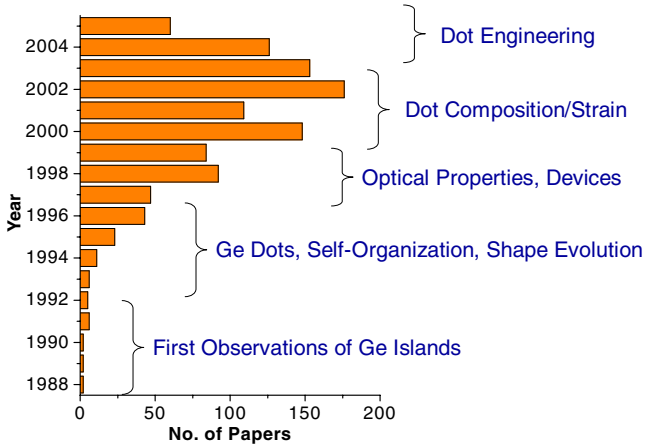

Figure 1. A sampling of papers discussing the synthesis, characterization and utilization of Ge dots and $Si_{1-x}Ge_x$ islands. Over the years, the emphasis of work in this area has evolved along the research trends indicated.

2. Experimental details

2.1. Epitaxial growth

The various $Si/Si_{1-x}Ge_x$ heterostructures that are specifically discussed here were prepared on (001) Si by MBE (VG Semicon V80) or by UHV-CVD (Leybold Syrius). The reader is referred to previous work for details on the MBE [13–17] and UHV-CVD [18–20] growth methodologies. The MBE Ge dots were typically obtained by depositing Ge monolayers at a temperature of about 650 °C and growth rate of 0.05 nm s^{-1}. The $Si/Si_{1-x}Ge_x$ island superlattices prepared by MBE [17, 21] consist of 10, 15, or 20 periods of alternating Si and $Si_{1-x}Ge_x$ layers. The Si layers in the structures have a nominal thickness of 13 nm, while the $Si_{1-x}Ge_x$ layers have a nominal thickness ranging from 3 to 5 nm and Ge composition x ranging from 0.3 to 0.55. Two growth temperatures were investigated, namely, 675 and 625 °C. A set of superlattices grown at 600 °C with $x = 0.15$ with varying alloy layer thickness was also prepared to track the morphological evolution of strained alloys. Most of the samples were terminated at the surface by a $Si_{1-x}Ge_x$ alloy layer to enable the study of the alloy surface morphology. Some samples were also terminated with a Si layer to investigate the effectiveness of a silicon cap in smoothing the surface. The UHV-CVD grown samples consist of a series of 10-period $Si/Si_{1-x}Ge_x$ superlattices with a nominal Ge composition of $x = 0.5$, Si spacer layers of 11 nm nominal thickness, and an alloy layer thickness in the range 3–8 nm. These were grown at 525 °C, with deposition rates of 1.2 nm min^{-1} for the Si spacer layers, and of 4 nm min^{-1} for the $Si_{0.5}Ge_{0.5}$ layers. All the UHV-CVD grown samples were terminated by a $Si_{0.5}Ge_{0.5}$ layer at the surface.

2.2. Characterization techniques

The transmission electron microscopy (TEM) was performed on a JEOL JEM-2100F field emission source transmission electron microscope operating at 200 kV. For the present study high angle annular dark field (HAADF) scanning TEM images were obtained using a Fischione annular dark field detector attached to the JEM-2100F to enhance chemical contrast in SiGe heterostructures. The chemical composition of the various Si/Ge nanostructures was

further studied quantitatively by the TEM analytical techniques of energy-dispersive x-ray spectroscopy (EDS) using an Oxford INCA Energy TEM 200 attached to the JEM-2100F and electron energy loss spectroscopy (EELS) using a Gatan GIF Tridiem attached to the JEM-2100F. The EDS spectra were calibrated by probing thick $Si/Si_{1-x}Ge_x$ heterostructures of known germanium composition.

Atomic force microscopy was performed with a Nanoscope III operated in the tapping mode. X-ray diffraction experiments were carried out on a Panalytical MRD system where $(\bar{1}\bar{1}3)$ reciprocal lattice maps were recorded in a grazing exit angle geometry, following the methodology described elsewhere [22–24].

The Raman scattering experiments were carried out in an ambient atmosphere of helium at a temperature of 295 K in a quasi-backscattering Brewster-angle geometry [25] with the incident light at an angle of 77.7° from the normal to the (100) surface. Spectra were excited with 100 mW of 457.9 nm argon laser light. The incident laser light formed a slit shaped spot of dimensions 1×0.1 mm^2 on the sample, which together with the use of the stream of He gas flowing over the sample in the laser spot area helped minimize the local laser heating. The light scattered at 90° (external to the sample) was analysed with a Spex 14018 double monochromator at a spectral resolution of 7.8 cm^{-1}, and detected with a cooled RCA 31034A photomultiplier. The incident light was polarized in the scattering plane, while the scattered light was recorded without polarization analysis. Spectrometer calibrations were made immediately before and after each sample spectrum was recorded.

Photoluminescence spectra were recorded using a Fourier transform infrared spectrometer with the samples immersed in cold helium gas ($T \sim 4.5$ K). The excitation wavelength was 514 nm (Ar^+ laser) and the power density at the sample was 10–100 mW cm^{-2}. The luminescence was measured with a germanium or InSb detector, which have a good responsivity in the wavelength regime of interest (i.e. 1.5 μm and higher).

3. Ge dots and $Si_{1-x}Ge_x$ islands

3.1. Nucleation, growth, and shape evolution of Ge dots on (001) Si

The development of strained-layer epitaxy in the early 1980s has made possible the synthesis of defect-free lattice mismatched semiconductor heterostructures. This has led to the development of a new class of semiconductor devices in which the band structure is tailored by the composition and strain distribution [26]. Maintaining 2D morphology and avoiding strain relaxation by limiting the thickness of heterostructures were key requirements enabling the fabrication of devices based on strain engineering. Growth conditions leading to 3D morphology were generally avoided due to requirements in device fabrication and detrimental effects on device performance. Heteroepitaxy in the regime favouring non-planar growth is, however, an attractive 'bottom-up' approach to synthesize novel structures at the nanometre scale without resorting to lithographic techniques. By optimizing growth parameters, it is possible to fabricate self-organized semiconductor nanostructures and possibly tailor their physical properties [11].

The (001) $Si/Si_{1-x}Ge_x$ heterostructures are prototypical examples of such self-assembled island systems. Ge dots and $Si_{1-x}Ge_x$ islands were first reported in the late 1980s [1–5, 15] and can be synthesized by most epitaxial growth techniques. Figure 2(a) shows an example of large Ge dome islands grown on (001) Si by MBE. The development of a 3D morphology arises when growth conditions allow sufficient surface adatom mobility, but limited bulk interdiffusion, and correspond to atomic configurations that minimize the system energy. The atoms at the top of the island are free to relax towards the bulk Ge lattice parameter and the elastic energy released exceeds the increase in surface energy.

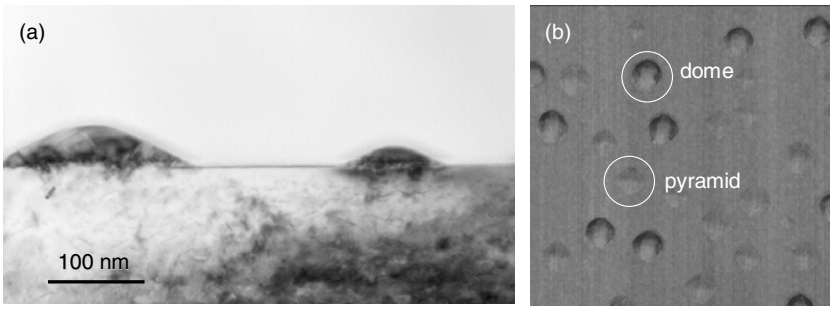

Figure 2. (a) Early observation [15] in a TEM image taken in 1987 of Ge dome islands on (001) Si grown at 650 °C. (b) Atomic force image of the surface topography of Ge islands on (001) Si grown by MBE at 650 °C showing the co-existence of pyramid-like and dome-shaped islands.

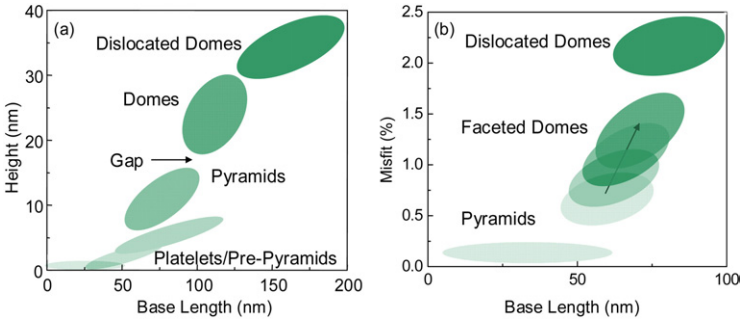

Figure 3. Generic Ge dot distribution on (001) Si with Ge coverage shown (a) in a dot height versus base length diagram and (b) in a strain versus dot base length diagram.

The evolution of $Si_{1-x}Ge_x$ islands with coverage has been studied extensively, and although variations are seen between the growth techniques Ge dots evolve following the sequence illustrated in figure 3(a). Pure Ge growth proceeds via the Stranski–Krastanow growth mode [27] with the formation of a 2D wetting layer (WL) of ∼3 ML followed by the growth of small 2D platelets or pre-pyramids [28] as the Ge coverage increases. Further deposition leads to the formation of well defined square or rectangular pyramids (also referred to as hut clusters) [5], with side walls oriented along [105] crystallographic directions. As the Ge coverage increases, large dome islands form on the surface. The surface of the domes exhibits various crystallographic facets that undergo a series of morphological transformations with coverage. With further increase of the Ge coverage, strain-relaxed large domes (superdomes) are formed with misfit dislocations at their base. One important characteristic of this dot system is the co-existence of pyramid-like dots exhibiting {105} side walls and larger faceted dome islands, as illustrated in the atomic force microscope image in figure 2(b). Examples of dome and pyramid islands are shown in TEM cross-sectional micrographs in figure 4. The coexistence of pyramids and domes leads to a characteristic bimodal dot distribution. The pyramid dots have a small aspect ratio and to a large extent retain the substrate lattice parameter in the surface plane (i.e. low in-plane misfit). As they evolve into domes, their aspect ratio decreases and relaxation of the lattice constant towards bulk Ge takes place (see figure 3(b)). The domes, which are initially coherently strained, evolve into strained relaxed larger domes (superdomes) as the coverage is increased up the point where the built-in stress can no longer be sustained. Real time studies of the island evolution during growth or upon annealing have revealed a complex transition from island to dome involving different

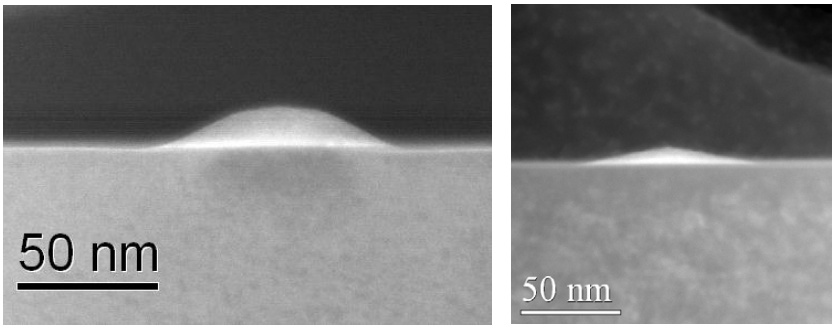

Figure 4. HAADF STEM images of (left panel) a Ge dome island and (right panel) a pyramid island formed on (001) Si after depositing 6 ML of Ge at 650 °C.

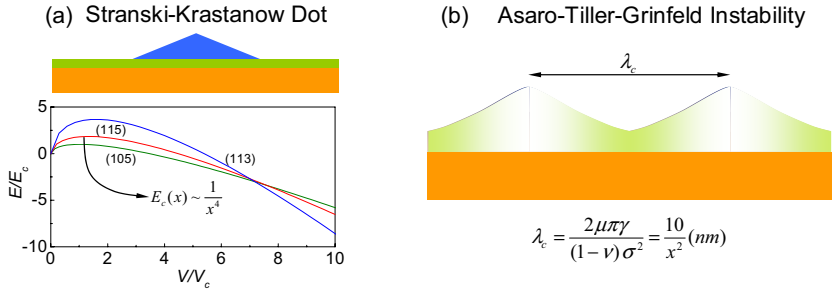

Figure 5. Schematic illustration of two mechanisms leading to 3D growth in strained systems. (a) Stranski–Krastanow growth where the volume dependence of the formation energy is plotted for three different facets using equation (1) with γ_s and γ_p set to 8 eV nm^{-2} and normalized to the critical values for the {105} facet (adapted from Tersoff and LeGoues [30]). (b) Asaro–Tiller–Grinfeld instability leading to undulated interfaces with critical wavelength λ_c.

intermediate configurations with decreasing aspect ratio [29]. The interplay of energetics and kinetics is key in determining the dot evolution.

The evolution from 2D platelets to pre-pyramid and then faceted pyramids may be explained by simple energetic considerations [30]. In the framework of the continuum approximation, the creation of a faceted island requires an energy E that depends on the island volume, surface free energy, misfit strain, and facet angle θ according to the expression [30]

$$E = 4\Gamma V^{2/3} \tan^{1/3}\theta - 6AV \tan\theta \tag{1}$$

where $\Gamma = \gamma_s \csc\theta - \gamma_p \cot\theta$ is the increase of surface energy, γ_s and γ_p are the surface energy per unit area of the wetting layer and pyramid facet, respectively, V is the volume of the pyramid, $A = \sigma_\parallel^2(1-\nu)/(2\pi G)$ where $\sigma_\parallel$ is the in-plane misfit stress, and ν and G are the Poisson's ratio and shear modulus of Si, respectively. This energy increases to a maximum E_c at a critical volume V_c and decreases at larger volume. E_c thus represents an activation energy for island nucleation that depends on the facet orientation. For the Ge on (001) Si system, the formation of {105} facets has the lowest activation energy (see figure 5) and thus explains the transition from 2D platelets to {105} pyramids [30]. Note that E_c increases as $1/\varepsilon^4$ (or here as $1/x^4$) and will become exceedingly high in a low-strain system, making the transition to the Stranski–Krastanow 3D growth mode unfavourable. Equation (1) predicts that there is no stable island size since once an island is nucleated; E decreases with increasing volume. The above formalism however neglects the effect of stress on the surface energies. An additional

negative term to account for stress discontinuity at the edge of the island facets could result in a minimization of E for a given island size [31]. Recent calculations for the SiGe system suggest that surface stress and edge effects may lower the activation energy for island formation, but the effect is too small to result in growth of islands of stable size [32, 33].

As illustrated in figure 5(a), steeper facets may become energetically favourable as the size of the dots increases, leading to pyramids with larger aspect ratios and eventually faceted domes, as depicted in figure 4(b). As more Ge is deposited, the pyramid dots thus evolve discontinuously into larger dome-shaped islands with steeper facets such as {113} and {111} (see figure 3(a)). This island evolution has been studied theoretically [34] and explained as a first-order shape transition controlled by the total surface energy of the faceted system: as the island volume increases, different faceted island shapes form to minimize free energy. This model has recently been corroborated in a systematic study of island shape evolution for the Ge–(001) Si and InAs–(001) GaAs systems, which showed in both cases the coexistence of pyramid- and dome-like islands [35, 36].

The influence of growth parameters and the effect of post-growth treatment such as annealing or capping on the properties of Ge islands have been studied extensively and we summarize next the key findings. The average size of the Ge islands grown by MBE increases with growth temperature [37] and the size distribution becomes narrower [38]. Coarsening of the islands is also observed upon post-growth annealing, dominated by the Ge consumption of the wetting layer at low temperature (450 °C), Si/Ge interdiffusion at intermediate temperatures (550 °C), Ostwald ripening at high temperature (650 °C) [39, 40], and abnormal Ostwald ripening at very high temperature (750 °C) [41]. In the latter case, the superlinear island coarsening reported has been explained by the initial broad size distribution of islands [42]. Annealing experiments at 550 °C have also suggested the existence of preferred configurations for both pyramid and dome islands [43]. Ge islands deposited at a lower rate will be larger and less dense than when deposited at a high rate [44]. Some island ordering has also been reported in Ge films deposited at a fast rate, while dome formation was inhibited at small separation at low deposition rates possibly due to the existence of a denuded zone around islands [45]. Depositing a Si cap at low temperature (300 °C) has been found to be a good means to preserve the shape of the islands [46, 47]. However, the overgrowth of the Ge islands by Si at high temperature may affect the island morphology. For example, when capped at a 700 °C temperature, pyramid dots have been observed to dissolve into the wetting layer [48] while larger domes were found to flatten upon Si capping at similar high temperatures [48–50]. At an intermediate temperature of 450 °C, capping Ge domes with monolayers of Si has revealed a transition of the dome into large pyramids that evolve into stepped mounds [46]. This shape reversal was explained by the incorporation of Si into the island which increases the critical volume for transition of the pyramid islands to dome islands [35, 36]. Despite the fact that bulk diffusion is low at this temperature, Ge surface diffusion and segregation is sufficient to reduce the strain in the system favouring morphologies with larger aspect ratios. Kinetic factors such as growth rate and deposition time or surface effects (presence of steps, of a surfactant, etc) are also likely to influence the details of this morphological evolution. These various results illustrate how some control on the structural properties of Ge islands can be achieved by optimizing growth parameters or performing post-growth treatments. An alternative approach to tailoring island formation and morphology is via the control of the host substrate through patterning or surface treatment, as is discussed later.

3.2. Critical thickness to 3D growth transition

In dilute $Si_{1-x}Ge_x$ alloys, as the composition and thus built-in strain is reduced, the transition to 3D growth is observed at increasingly larger thicknesses [51] and a similar phenomenon is

observed in other hetero-epitaxial systems such as $In_{1-x}Ga_xAs$ layers grown on GaAs [52, 53]. In the latter case, the onset for 3D growth was correlated with the build-up of the In concentration (and consequently surface stress) in the surface region above that expected from the ratio of incoming atomic fluxes [53]. It has been proposed that it is only when the In surface concentration reaches a critical value (about 80 at.%) that the 3D growth transition can take place. In this picture, the critical thickness of the 3D transition should increase for more dilute alloys, but should be relatively insensitive to the growth rate, as observed experimentally. Calculations based on a continuum model [54] show that indeed, due to intermixing in the surface region, the $Si_{1-x}Ge_x$ alloy surface concentration of a deposited alloy remains initially below the nominal concentration. It is only when the alloy concentration in the surface region reaches a threshold value that the film becomes unstable to 3D growth. Surprisingly, the model also shows that surface segregation can actually increase the critical thickness for the growth transition since it tends to lower the effective alloy concentration of the intermixed layer underneath the surface. The model can reproduce the observations for $In_{1-x}Ga_xAs$ layers, but awaits experimental corroboration for the SiGe system.

3.3. Undulated interfaces and Si/$Si_{1-x}Ge_x$ island superlattices

As pointed out above, in low strain hetero-systems, the Stranski–Krastanow growth mode is not energetically favourable. However, a growing stressed surface is unstable against surface roughening and this may also lead to growth exhibiting a 3D morphology. This strain-induced roughening of a thin epitaxial film is generally known as the Asaro–Tiller–Grinfeld instability [7, 55]. For a hetero-epitaxial film under compressive stress, undulation of the surface allows lattice planes to relax towards the ripple peaks (see figure 5(b)). This lowers the elastic energy stored in the film, but increases the surface energy as compared to a planar surface. The balance between the reduced stress and increased surface energy defines a critical minimum wavelength λ_c for stable undulations given by [56]

$$\lambda_c = \frac{2\mu\pi\gamma}{(1-\nu)\sigma^2} = \frac{(1-\nu)\,\pi\gamma}{(1+\nu)^2\,\varepsilon^2} \tag{2}$$

where γ is the surface energy density, ε and σ are the misfit strain and stress, respectively, μ is the shear modulus, and ν is Poisson's ratio of the film. Note that the morphological instability scales here as $1/\varepsilon^2$ (or here as $1/x^2$), which makes this process effective in low strain systems prior to Stranski–Krastanow dot formation. Surface undulations of wavelength larger than λ_c can form via surface diffusion to minimize the system energy. Conversely, for wavelengths smaller than λ_c, it is energetically favourable to fill surface troughs to reduce surface energy and thus smoothening is expected. In the case of a $Si_{1-x}Ge_x$ film on (001) Si, Ge atoms are expected to migrate towards the crest of the undulations where the lattice constant is closer to that of bulk unstrained $Si_{1-x}Ge_x$ material. Using the elastic constants of Si and Ge [57], equation (1) yields λ_c of the order of 100 nm for a $Si_{0.50}Ge_{0.50}$ alloy layer on (001) Si.

Stacked islands or undulated superlattices can be obtained by depositing alternating layers of strained islands and thin substrate material spacers in near-equilibrium growth conditions (such as low growth rate or high deposition temperature) promoting the Asaro–Tiller–Grinfeld morphological instability. This is a good means to increase the total volume of 3D nanostructures without incurring strain relaxation via plastic deformation (i.e. injection of misfit dislocations). In general, island superlattices exhibit a strong vertical correlation and the stacking morphology may be mediated by the strain field, residual non-planar morphology or non-uniform chemical composition of the spacer layer as has been recently discussed in detail elsewhere [58].

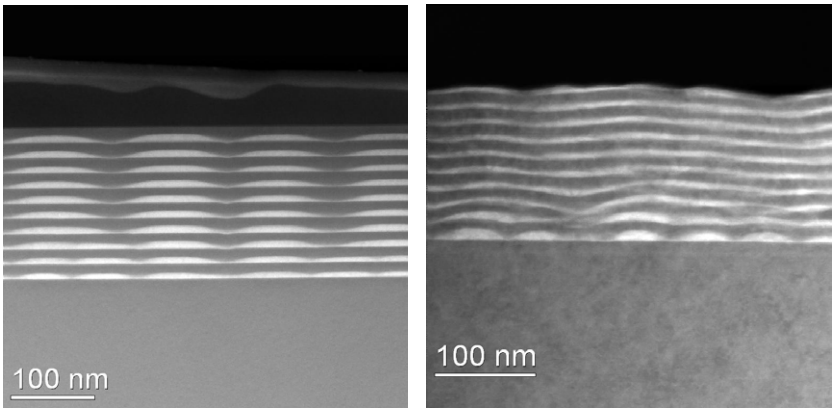

Figure 6. HAADF STEM cross section images of island superlattices grown by (left panel) MBE ($Si_{0.54}Ge_{0.46}$/Si superlattice with 3.4 nm thick alloy layers and 13.7 nm Si spacers, grown at 625 °C) and (right panel) UHV-CVD ($Si_{0.4}Ge_{0.6}$/Si superlattice with 4 nm thick alloy layers and 12.5 nm Si spacers, grown at 525 °C).

Examples of $Si/Si_{1-x}Ge_x$ undulated superlattices grown by MBE [16] or UHV-CVD [20] are presented in figure 6. The micrograph in panel (a), obtained from an MBE grown structure, shows extremely regular undulations forming at the alloy to Si interfaces. In the Si–Ge system, the vertical alignment of the islands arises from a partial elastic relaxation of the $Si_{1-x}Ge_x$ lattice at the apex of the island, which causes tensile strain in the Si lattice above the $Si_{1-x}Ge_x$ island [58]. This locally reduces the misfit strain and makes it an energetically favourable nucleation site for a $Si_{1-x}Ge_x$ island in the next alloy layer. This vertical alignment may be lost if the Si spacer layer thickness is increased to the extent that negligible strain exists at the surface. The critical spacer thickness depends on the growth methods and conditions [7] but, in general, strong vertical alignment is achieved for spacers less than 25 nm thick, while little alignment is preserved beyond 100 nm [59, 60]. The degree of vertical ordering has been correlated with a reduction of the thickness of the WL in stacked islands, which is also consistent with strain propagation in the Si spacers [61]. The coarsening and coalescence of islands in the upper layers of island superlattices (see figure 6) is a self-organization process that may be explained in the framework of continuum elasticity theory [62]. The strain field overlap of two closely spaced small islands will result in the nucleation of a larger island in the next alloy layer rather than the replication of the small islands, while for larger islands the strain field will not expand beyond the lateral size of the islands and their size will be self-limited. Finally, some oblique stacking of islands is sometime observed and has been explained by the interplay of surface stress and the development of Si surface depressions (step-bunching) in the vicinity of large islands [63]. No well ordered staggered stacking has been observed in the Si–Ge system on (001) Si, because elastic anisotropy favours vertical alignment [58].

Island superlattices prepared by UHV-CVD exhibit different interface morphology as can be seen in panel (b) of figure 6. Although a self-regulation of the Ge island size is again observed, here both types of interfaces (i.e. alloy to Si and Si to alloy) exhibit a similar waviness. In contrast to the MBE case, this results in structures exhibiting undulated layers with no appreciable thickness variations in the plane of growth. The difference may be due to the lower growth temperature used in UHV-CVD and to the conformal nature of this growth technique. Here the vertical stacking is probably influenced by strain and the non-planarized topography of the spacer layers. The presence of atomic hydrogen on the surface has been

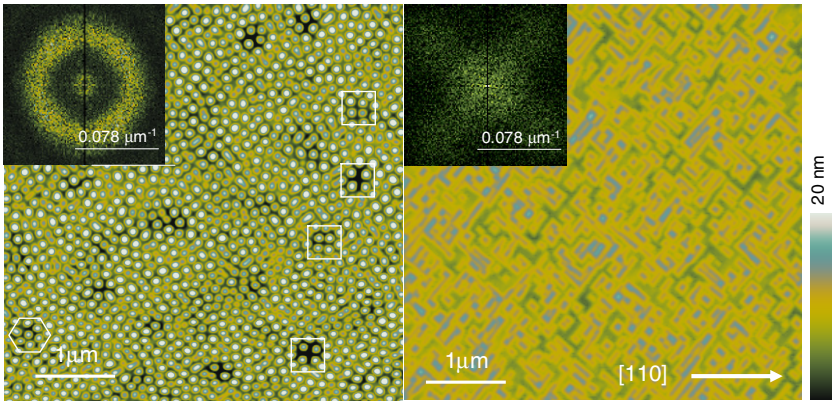

Figure 7. AFM images showing the surface morphology of $Si/Si_{1-x}Ge_x$ island superlattices prepared by (left panel) MBE and consisting of ten periods of 13 nm Si/3.4 nm $Si_{0.54}Ge_{0.46}$ and (right panel) UHV-CVD and consisting of ten periods of 15 nm Si/3 nm $Si_{0.50}Ge_{0.50}$. The inset is a power spectral density map of the image.

shown to enhance Ge surface diffusion in MBE [64] and this effect may also contribute to the disappearance of well defined islands in UHV-CVD growth.

The long-range organization of islands in island superlattices in the plane of growth is best revealed by surface probe techniques. Figure 7 displays the surface morphology of alloy-terminated $Si_{1-x}Ge_x$ island superlattices grown by MBE and UHV-CVD as obtained by AFM. The MBE grown superlattice exhibits a rough surface morphology comprising dome-shaped mounds that are predominantly aligned along the [100] and [010] directions. The shape of these mounds is independent of the Ge composition in the range investigated, but their average size decreases with increasing growth temperature. The surface root mean square (RMS) roughness of MBE grown superlattices is typically 4 nm. The preferred size and orientation of the surface undulations are clearly seen in a Fourier transform of the surface topography shown in the inset in figure 7(a). The well defined size of the surface mounds and their dome shape is revealed in the Fourier image by the presence of a ring of constant reverse length and little azimuth dependence. A weak fourfold symmetry of the Fourier image revealed by a higher intensity along ⟨001⟩ directions is consistent with the preferential orientation of the island facets along these crystallographic axes. The weak intensity in the centre of the power spectrum density map indicates the absence of surface domains with [001] orientation. The surface topography also exhibits short range ordered structures such as those circled in figure 7(a). Such ordered structures have been observed in $Si_{0.55}Ge_{0.45}$ islands on vicinal (001) Si substrates and have been explained by the interplay of step-bunching and strain-driven island growth [65–67].

Stacked $Si/Si_{1-x}Ge_x$ island superlattices grown by UHV-CVD exhibit a different surface morphology. Elongated mounds meandering along [100] directions are observed on the surface (RMS roughness of 2.5 nm). This morphology is very similar to that reported on single-layer $Si_{1-x}Ge_x$ alloys grown by high temperature low pressure vapour deposition [68]. The Fourier transform of the AFM image exhibits a stronger fourfold symmetry with distinct lobes oriented along [100] directions. The alignment of the surface features is better defined here since no continuous ring is seen in the Fourier spectrum. Also, a strong signal at the centre of the spectral power density map indicates the presence of regions with [001] orientation on the surface between the islands.

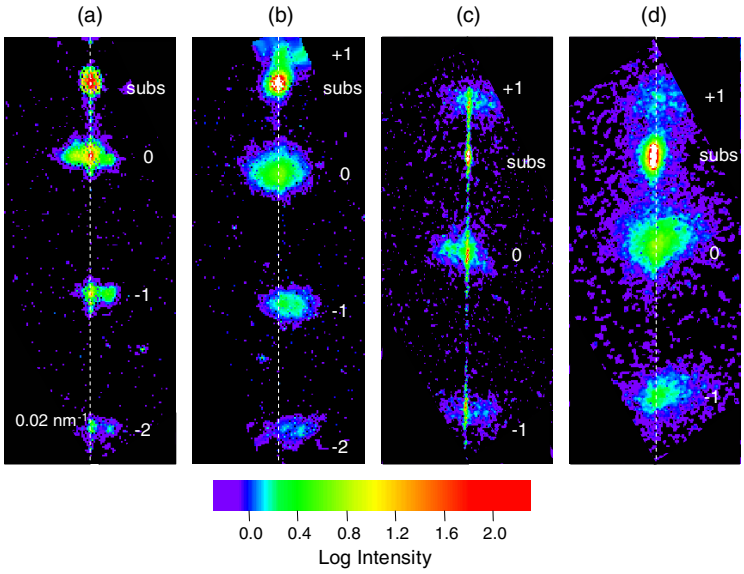

Figure 8. Reciprocal space maps from island superlattices. Maps from panels (a) and (b) were obtained from MBE grown superlattices deposited at 625 °C and consisting of 20 periods of 14 nm Si/3.5 nm $Si_{0.54}Ge_{0.46}$ and 15 periods of 14 nm Si/3.6 nm $Si_{0.45}Ge_{0.55}$, respectively. Maps from panels (c) and (d) were obtained from UHV-CVD grown superlattices deposited at 525 °C and consisting of 10 periods of 14 nm Si/3.5 nm $Si_{0.58}Ge_{0.42}$ and periods of 12.5 nm Si/4.0 nm $Si_{0.45}Ge_{0.55}$, respectively. More details on the measurements are presented elsewhere [16].

The undulating nature of the interfaces in $Si/Si_{1-x}Ge_x$ island superlattices can be revealed by high resolution x-ray diffraction reciprocal lattice mapping. Figure 8 compares reciprocal space maps measured on representative samples. Details of the x-ray measurements can be found elsewhere [14, 24]. These maps were acquired using the very asymmetric $(\bar{1}\bar{1}3)$ reflections in a low exit-angle geometry to enhance diffraction effects due to undulations in the plane of growth [14]. The maps exhibit the usual satellite peaks in the vertical direction associated with the super-periodicity of the structures. The alignment of the satellite peaks in the same vertical line as the substrate peak indicates that the structures have retained their strain despite the presence of interface undulations. In addition, secondary features are seen in the horizontal direction beside the superlattice peaks. These side lobes are associated with the lateral periodicity of the interfaces. The side lobes are seen on both MBE and CVD grown samples (figures 8(a) and (c)), although for the latter they are generally not as intense or well defined. With both growth techniques, the side lobes become unresolved in structures with high Ge fraction ($x > 0.5$) and the main satellite peaks become broader (panels (b) and (d)). For structures grown by MBE, the satellites tend to broaden along the wavevector parallel to the surface, indicating a decrease of the coherence length of the superlattice in the plane of growth. The corresponding satellites from the UHV-CVD superlattice (figure 8(d)) tend to broaden in both wavevector directions parallel and perpendicular to the surface, indicating the loss of super-periodicity and a reduced coherence length. In general, diffuse scattering is stronger in structures grown by UHV-CVD, consistent with a weaker self-organization of the interface undulations. X-ray reflectivity measurements [16] have also shown that, in general, MBE grown island superlattices retain a better vertical correlation, as can also be seen in the TEM micrographs of figure 6.

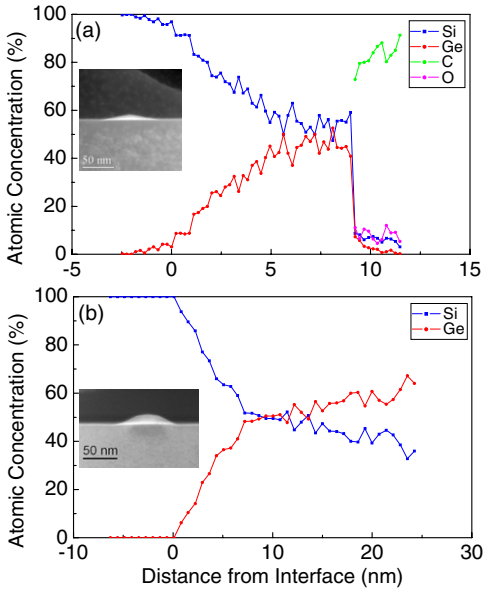

Figure 9. EDS chemical profile in the growth direction for (a) a pyramid-like SiGe dot and (b) a dome dot. The spectra are from the same sample, obtained by MBE by depositing 5 ML of Ge on (001) Si at 650 °C.

3.4. Composition and strain distribution

The determination of composition and strain in Ge dots and $Si_{1-x}Ge_x$ islands has been the subject of a number of recent investigations, as reviewed in detail elsewhere [11, 12]. X-ray techniques in particular have provided insight on this question. Simulation of the intensity distribution of the diffraction signal from dot structures has shown that for uncapped Ge dots grown at 600 °C, the Ge concentration decreases from nearly 100% at the island apex to 50% at the base of the island [69]. For Si-capped islands grown at 700 °C, a similar trend was seen with the Ge concentration reduced to 78% and 37% at the apex and base, respectively [70]. Anomalous x-ray scattering measurements [71, 72] have revealed that the vertical decrease in the Ge concentration with height was rather abrupt and occurred in the first 2 nm from the surface. Moreover, in Ge dome islands, the Ge concentration was found to vary with height and was consistent with a structure made of a Si-rich core covered by a Ge-rich shell [73]. In the case of stacked Ge islands, a similar Ge increase was observed at the apex of the islands and the average Ge concentration in the islands was found to decrease in the upper layers possibly due to strain enhanced diffusion [74, 75].

Analytical TEM techniques have recently been used to investigate the structure and composition of Ge nanostructures [76–81]. Here, the composition profile of pyramid and dome Ge dots grown by MBE has been investigated by STEM-EDS and the results are found to be consistent with those outlined above. Figure 9 displays the Ge concentration profile in the growth direction for the two types of dots formed upon deposition of ∼5 ML of Ge on (001) Si at 650 °C. For a pyramid dot (figure 9(a)), considerable Si–Ge intermixing is observed, with the dot Ge concentration increasing almost linearly from close to zero at the base of the dot to about 0.5 at the apex of the pyramid. EDS scans in the direction parallel to the interface show that the Ge concentration at a given height is uniform across the pyramid, with perhaps a small decrease at the dot edges [82]. The dome dots show a different concentration profile as shown

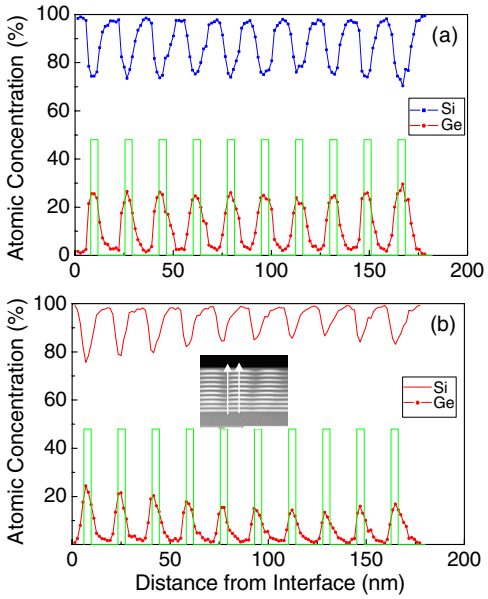

Figure 10. EDS chemical profile in the growth direction for a ten-period $Si_{0.52}Ge_{0.48}$ (3.7 nm)/Si (13.7 nm) island superlattice grown by MBE at 625 °C and measured (a) along an interface crest and (b) along an interface valley, as shown in the micrograph in the inset. Also indicated on the graph (by vertical bars) is the nominal Ge concentration profile based on the growth parameters.

in figure 9(b). The Ge concentration presents a more pronounced gradient at the base of the dot and already reaches about 0.4 at a 5 nm height. Beyond that point, the Ge concentration only builds up slowly to reach about 0.6 at the top of the dome. Those results corroborate earlier analyses that point to considerable intermixing in dots grown at high temperatures. They are consistent with an EELS study of the Ge island concentration of dome islands as a function of temperature [83]. In the case of dome dots, the Ge concentration at a given height was found to be remarkably uniform laterally and this would not support the model of a Si-rich core and Ge shell inferred from x-ray scattering studies [73]. Details of these measurements will be presented elsewhere [82].

The concentration profile in the growth direction in island superlattices was also investigated by STEM-EDS. Figure 10 compares the Ge profiles in the growth direction measured along (a) a crest and (b) a trough of an MBE grown island superlattice with $x = 0.48$. As was observed in the dot structures, considerable Si–Ge intermixing takes place in the island superlattice. The Ge peak concentration in the crests is only about 0.2 or half the nominal Ge concentration expected from the deposition rate. The integrated Ge signal per superlattice period is, however, close to that of the nominal structure. In the troughs, the Ge concentration is significantly reduced and the integrated Ge signal corresponds to approximately 50% of that of a nominal superlattice period, indicating significant surface lateral diffusion during growth. Moreover, the Ge profiles in figure 10 clearly point to Ge surface segregation, as evidenced by an exponential decay of the Ge concentration at the trailing edge of the SiGe layers. Here the decay length is about 3.3 nm, in good agreement with values of the decay length found in planar $Si/Si_{1-x}Ge_x$ heterostructures [84, 85]. The decay of the total Ge content in successive troughs also indicates higher chemical contrast and better defined Ge-rich islands as growth progresses.

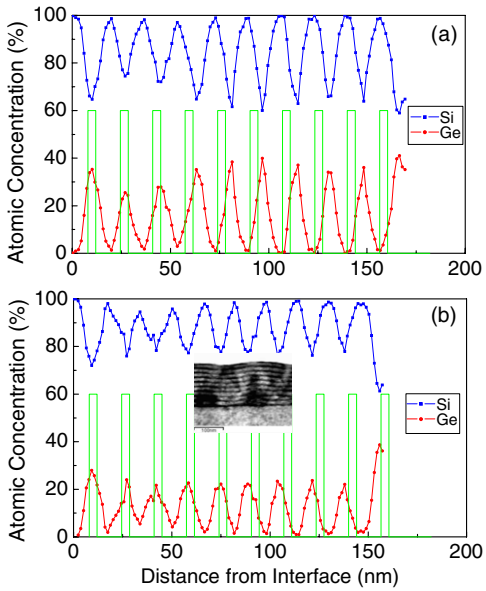

Figure 11. EDS chemical profile in the growth direction for a UHV-CVD grown ten-period $Si_{0.60}Ge_{0.40}$ (4.0 nm)/Si (12.5 nm) island superlattice measured (a) along an interface crest and (b) along an interface valley, as shown in the micrograph in the inset. Also indicated on the graph (by vertical bars) is the nominal Ge concentration profile based on the growth parameters.

A similar STEM-EDS analysis performed on a UHV-CVD island superlattice revealed interesting differences as illustrated in figure 11. Here the Ge profile in each superlattice period exhibits a symmetrical triangular shape, suggesting that interdiffusion takes place at both the leading and trailing interfaces of the $Si_{1-x}Ge_x$ alloy layers. The decay length of the Ge concentration is about 2.5 nm and there seems to be no appreciable Ge segregation, possibly because of the surfactant effect of hydrogen created by dissociation of silane and germane. For the line scan performed along a superlattice crest, the integrated Ge signal is equivalent to a Ge composition of 0.48, which is less that the nominal composition of 0.6, based on growth parameters. In comparison, the line scan along a trough shows a depletion of the Ge signal that corresponds to an equivalent Ge concentration of 0.35. Some variations in the Ge composition from period to period are also seen in the UHV-CVD sample. The lower average Ge composition is explained by a non-linearity between the Ge incorporation rate and germane flow rate [18]. The undulation of both types of interfaces progressively leads to a loss of registry of the superlattice period with respect to the nominal structural parameters, a phenomenon that is not observed by MBE.

Strain in individual islands is best measured by microscopic techniques such as TEM. Strain contrast from TEM images of pyramid and dome islands reveals that the latter are heavily strained (about 2%) with respect to the substrate, while pyramids are almost commensurate (i.e. tetragonally distorted, with a strain of less than 0.5%) with the substrate [86]. The difference in strain within domes and pyramids is illustrated in figure 12, which shows dark field TEM cross-sections recorded in two different two-beam conditions. The (400) two-beam condition is sensitive to lattice distortion in the growth direction and shows that considerable strain is induced at the periphery of and underneath the dome island over a region corresponding roughly to the size of the dot. In contrast, little evidence of strain in the substrate is seen in the

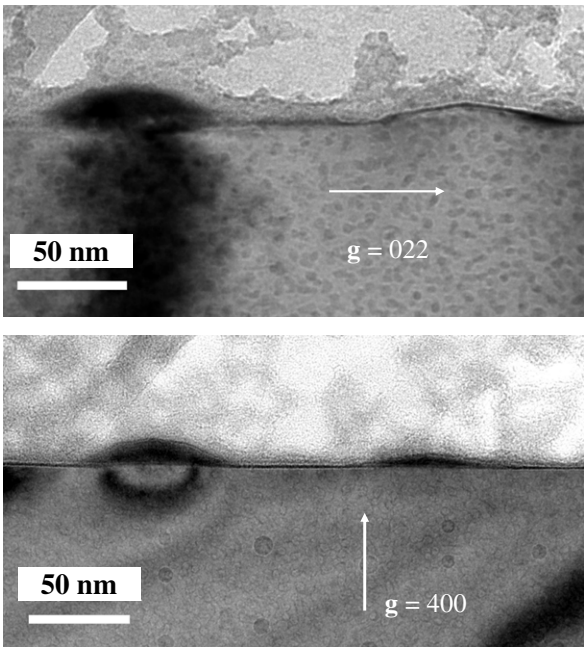

Figure 12. Bright field cross-section TEM micrographs showing a dome (left) and pyramid (right) dot and recorded in (022) and (400) two-beam conditions.

case of the pyramid islands. From the (220) two-beam condition, it is found that the presence of the dome also induces a bending of the lattice planes parallel to the surface centred on the dot and extending to an appreciable depth underneath the dot. Again, no evidence of lattice distortion is seen underneath a pyramid dot. Such strain gradients in $Si_{1-x}Ge_x$ dome dots have also recently been measured by quantitative high resolution TEM [87]. The discontinuous strain evolution between pyramid and dome dots is mediated by the formation of metastable dome-like islands with intermediate strain (see figure 2(b)). Stress calculations based on linear elastic theory have shown that besides the reduction of the strain energy, islanding also causes a strain concentration at the edge of the island [88]. The stress at the island periphery contributes to the self-regulation of island size by introducing a kinetic barrier to diffusion of adsorbed atoms onto the island. Concentration of stress at the edge of Ge dome islands has been confirmed by Fourier transform mapping of high resolution TEM images of Ge islands [89]. Molecular dynamics simulations of strain and stress distribution in Ge pyramids and domes [90] have reproduced these observations and shown that the Si lattice is significantly distorted below the edge of the Ge islands. As pointed out before, the strain gradient at the edge and underneath the island may enhance Si–Ge interdiffusion and thus alloying constitutes an alternative strain relaxation pathway for large Ge islands, especially when grown at high temperature or upon post-growth annealing [91]. Reduction of the stress energy at the edge of both pyramid and dome islands leads to the formation of a trench along the dot perimeter. This phenomenon is more pronounced at a higher growth temperature and the depth of the trench increases with the size of the islands and along [110] directions [92]. Microscopy imaging of the trenches [93] and recent modelling [94] suggest that the reduction of the concentrated stress below the edges of the islands is the driving force for trench formation. At high growth temperatures, Si surface diffusion over long distances can cause long range Si depletion around an island.

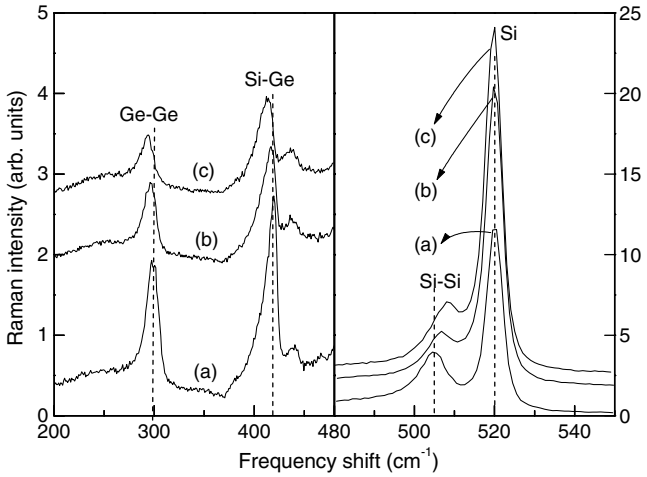

Figure 13. Room temperature Raman spectrum showing the optics modes of (a) a Si/$Si_{1-x}Ge_x$ planar superlattice for $x = 0.52$, (b) an island superlattice for $x = 0.56$, and (c) an island superlattice for $x = 0.45$ [99]. Dotted lines emphasize the shift of the main Raman lines.

3.5. Vibrational properties of Ge dots and $Si_{1-x}Ge_x$ island superlattices

Raman spectroscopy entails the inelastic scattering of monochromatic light from elementary excitations such as atomic or lattice vibrations, spin waves or magnons, and electronic excited states of some medium. In semiconductors, Raman spectroscopy can be used to provide information on the crystalline state and the presence of dopants and impurities [95]. In the case of semiconductor alloys, it can also be used to elucidate the alloy composition [96, 97]. Raman scattering is particularly well suited to studying the electronic and vibrational properties of thin layer semiconductor heterostructures and superlattices and has been widely applied to obtain information such as lattice strain and hetero-interface sharpness and composition [98]. This is because the lattice vibrational energies, which are governed by short range forces between atoms, are very sensitive to atomic bond lengths and angles and atomic masses. Because of the law of wavevector conservation, only excitations at very small wavevectors are probed in first-order Raman scattering.

Raman spectroscopy has been widely applied to characterizing the strain and composition of $Si_{1-x}Ge_x$ dots grown on Si by a variety of growth methods ranging from MBE to CVD [16, 99–135]. The crystal structures of Si and Ge are the same as that of diamond and consist of two interpenetrating face-centred-cubic lattices. This structure yields one triply degenerate optical mode of vibration at zero wavevector at a frequency of 1330, 520, and 300 cm^{-1} in C (diamond structure), Si, and Ge, respectively, at room temperature. This mode is strongly Raman active, which makes these materials ideal for Raman characterization studies. Alloys of Si and Ge [99] and Si and C [136] are more complicated, however. They possess three clearly separated optic modes of vibration, which are termed the A–A, A–B, and B–B modes (where A is Si and B is Ge or C) by association with the dominant bond interaction that produces them. In the Raman spectrum of $Si_{1-x}Ge_x$ these modes appear at approximately 505, 415, and 295 cm^{-1}, as shown for example in figure 13. By measuring the peak frequencies of these modes as a function of the Ge concentration x, the results shown by the full lines in figure 14 are obtained. Here it can be seen that the Si–Si (Ge–Ge) mode frequency decreases (increases) linearly with x, while the Si–Ge mode behaviour is best represented by a fourth-order polynomial [99].

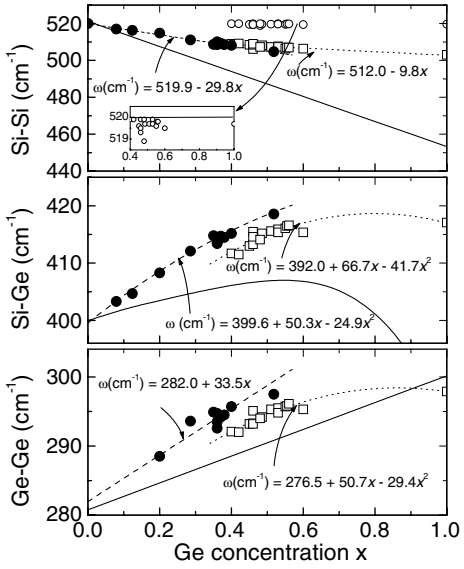

Figure 14. Frequencies of the three optic modes of $Si/Si_{1-x}Ge_x$ island superlattices (open squares) and planar superlattices (solid circles) as a function of composition x. The Si mode frequency from the Si layers in $Si/Si_{1-x}Ge_x$ island superlattices is given by the open circles and shown magnified in the inset. The solid lines are for bulk material [99].

All three optical modes are sensitive to the presence of strain, which causes a shift in their mode frequencies [137, 138]. Biaxial strain found in epitaxial layer growth on Si induces a phonon frequency shift $\delta\omega$ described by [137]

$$\delta\omega = \omega - \omega_o = \frac{1}{\omega_o}\left[\frac{pv}{v-1} + q\right]\varepsilon_\parallel = b\varepsilon_\parallel \tag{3}$$

where p and q are phenomenological parameters and $\varepsilon_\parallel = (a_{sub} - a_{epi})/a_{epi}$ is the lattice mismatch between Si and the $Si_{1-x}Ge_x$ epitaxial layer. Here, a_{sub} and a_{epi} are the bulk lattice constants of Si and $Si_{1-x}Ge_x$, respectively, and ω_o is the phonon frequency for zero strain. For the Si–Si mode, results for the strain-shift coefficient b measured as a function of x were fitted to a linear function, and the best fit was obtained with [137]

$$b\ (\mathrm{cm}^{-1}) = -715 - 825x. \tag{4}$$

The lattice constant a_{epi} of $Si_{1-x}Ge_x$ is well approximated by the quadratic equation [139]

$$a_{epi}\ (\mathrm{nm}) = 0.5431 + 0.02x + 0.0027x^2. \tag{5}$$

As a representative case study, we consider $Si_{1-x}Ge_x$ island superlattices with $0.4 < x < 0.6$ grown by MBE [99]. The $Si_{1-x}Ge_x$ islands in these superlattices are in the form of vertically correlated flattened domes (see figure 6) of typical dimensions ∼100 nm by ∼3.5 nm with a vertical spacing of ∼13 nm. Figure 13 presents representative optic mode spectra of $Si/Si_{1-x}Ge_x$ superlattices for three compositions $x = 0.45$, 0.52 and 0.56, where the samples of $x = 0.45$ and 0.56 are island superlattices and the sample of $x = 0.52$ is a planar superlattice, which is shown for comparison purposes. The spectra show four main peaks corresponding to the Ge–Ge, Si–Ge and Si–Si vibrational modes of the alloy layers and the Si optic mode of the Si layers of the superlattice. As can be seen in figure 13, the Ge–Ge and Si–Ge mode frequencies in both island superlattices are significantly less than those of the

planar superlattice, indicating a relaxation of the lattice constant toward unstrained bulk alloy values in the island superlattice compared with that in the planar superlattice. The Si–Si mode frequency in the island superlattice is found to have increased slightly compared with that in the planar superlattice. In general, the higher the proportion of Si there is in the $Si_{1-x}Ge_x$ alloy the shorter the Si–Si bond length [140], so that the Si–Si mode frequency shifts up. Therefore, the origin of this apparent inconsistency is related to an inhomogeneity in the Ge content within the alloy layers, as was revealed in the STEM-EDS analysis. In figure 14, the frequencies of the three optic modes are displayed as a function of x for the strained planar superlattice (solid circles) [138], island superlattice (open squares) and unstrained alloy (solid lines). In addition, the frequencies of the Si mode from the Si layers in the island superlattices are represented by the open circles, and the solid line in the inset indicates a bulk Si reference frequency of 520 cm^{-1}. The island superlattice Si-mode data lie just below the bulk Si frequency of 520 cm^{-1}, indicating the existence of a slight tensile strain in the alloy layers, as expected from the sample morphology. Note that the point at 518.9 cm^{-1} for $x = 0.48$ is from a partially relaxed island superlattice with an alloy layer thickness of 5 nm. The short dashed lines in figure 14 are from fits of the planar superlattice mode frequencies to linear and quadratic functions of x. The overall dependence on composition x of the island superlattice mode frequencies is represented by the long dashed line, which is a guide for the eye. It shows that the three mode frequencies in the island superlattice behave as a function of x quite differently from those in both the unstrained bulk and planar superlattices. This indicates that apart from strain and composition other factors such as island size, distribution, and shape [130, 133] might have to be taken into account in analysing the behaviours of the optic phonon mode frequencies in an island or dot nanostructure. As was discussed in previous work on $[Si_mGe_n]_p$ planar atomic layer [141], island [104, 105, 109] and dot [130] superlattices, where m and n are the numbers of Ge and Si monolayers in each of the p periods, the effect of phonon confinement could play an important role in determining the vibrational frequency of phonon modes in a given superlattice layer. In order to observe a noticeable frequency shift due to the effect of confinement, calculations [141] have shown that the layer thickness of $[Si_mGe_n]_p$ superlattices must be restricted to ultrathin layers of $m, n < 6$. In this study, the $Si_{1-x}Ge_x$ and Si layers typically have about 3.5 and 13.5 nm thickness, respectively, and this indicates that the effect of phonon confinement can be neglected. Also, the islands are of uniform size and shape. In figure 14, therefore, the x dependence of the deviations of the three mode frequencies in the planar and island superlattices from the frequencies of the three modes in the unstrained bulk alloy case has to be explained solely in terms of the strain and composition effects.

The results presented here are consistent with an accumulation of Ge at the crest of the undulations that will cause a decrease of the Ge fraction in the continuous alloy layers between the islands, causing a shift down in frequency for the alloy vibration modes. In fact, the vibrational frequencies in the undulated case are close to those measured in planar superlattices with a nominal Ge concentration about 10% less (see figure 14), consistent with analytical TEM results. In undulated superlattices there is also clear evidence of Ge diffusion into the Si in the limiting case of $x = 1$, i.e. the attempted growth of a pure Ge layer, where the Si–Si and Si–Ge modes can still be observed and the three mode frequencies are similar to their respective $x = 0.55$ values, as can be seen in figure 14. The out-diffusion of Ge results in Si-rich alloy regions in the valleys (between the $Si_{1-x}Ge_x$ crests) that are under compression. Both effects will raise the Si–Si line frequency above expected values.

Combining equations (3)–(5), we deduce a strain induced shift of $\delta\omega = 22.9$ cm^{-1} for the Si–Si mode in the planar superlattice of $x = 0.52$. Experimentally, from the peak position of the Si–Si mode in the $x = 0.52$ planar superlattice (spectrum (a) in figure 13) and the linear function for the Si–Si mode in the unstrained alloy given in figure 14, the frequency

shift $\delta\omega$ is estimated to be 19.0 cm^{-1}. This result is a little smaller than the predicted value, although it should be noted that the linear function for b was deduced from a fit of data obtained for $x < 0.35$ and some discrepancy could be expected at higher x values. Using the same procedure, one can calculate that $\delta\omega = 25.5$ cm^{-1} for the Si–Si mode of the $x = 0.56$ island superlattice, which compares favourably with the experimental value of $\delta\omega = 23.8$ cm^{-1}. The differences between these two sets of values are comparable, indicating that the average strain in the alloy layer of the island superlattice determined from Raman scattering can be evaluated in the same way as for the planar superlattice.

Annealing an MBE-grown $Si_{0.515}Ge_{0.485}$/Si island superlattice for 100 s at temperatures ranging from 700 to 850 °C had no observable effect on the optic and acoustic mode Raman spectrum [25]. This indicates that the island superlattice structure is quite resistant to interface atomic interdiffusion and strain relaxation under these annealing conditions. However, this is not the case for Ge dot superlattices containing smaller pyramidal-shaped dots [109, 111, 118, 125, 142]. Here, annealing for 1 h at 650, 700, and 800 °C resulted in a decrease in both the overall intensity and number of folded acoustic modes observed [125, 142]. This indicates that there exists a significant Si/Ge intermixing during the annealing process. A shift to lower frequency of the Ge–Ge and Si–Ge optic modes on annealing together with an increase in frequency of the Si–Si mode confirms that Si/Ge interdiffusion is occurring [109, 118, 125]. The difference in the thermal stability of the dome and pyramid superlattices is a reflection of the difference in their strain distributions, as discussed above. The Ge pyramids retain the substrate lattice constant parallel to the surface and may relax via dislocation formation at high temperature, whereas in the case for $Si_{1-x}Ge_x$ domes the strain distribution between the dots and the Si matrix is more equitable and plastic thus relaxation is less likely to occur.

In summary, and as has been shown in a number of studies [106, 107, 109, 112, 115, 118], [123, 125–127, 130–133, 135], the Si–Ge and Ge–Ge mode frequencies as a function of x in the dome superlattice show a decrease with respect to those in the comparable fully strained planar superlattice, which means that the average strain in the dome superlattice is reduced from that in the planar superlattice. The strain reduction can be appreciable [126, 131, 132]. However, the situation is reversed for the island Si–Si mode, which contradicts the case of the Si–Ge and Ge–Ge modes. The occurrence of such an apparent inconsistency is attributed to inhomogeneity in the alloy layers, caused by the sideways diffusion of Ge during the sample growth. The Si layer is thus under weak tensile strain above the domes and can be compressively strained between the domes [126], because of the growth conditions. It is also possible that for high Ge content domes, the Ge atoms form nanometre size clusters with a nearly pure Ge core surrounded by a $Si_{1-x}Ge_x$ shell [118, 121, 127], but the analytical TEM study presented here tends to invalidate this model.

Interestingly, Raman measurements of pyramid shaped Ge dots indicate that there can be no strain relaxation within the dots and, consequently, no strain transfer to the Si layers [106, 117, 126, 130]. These differences in the strain distribution in the Si layers correlate with the degree of three-dimensional ordering in the superlattice [8].

Finally, in this section, a cautionary tale. The Raman spectrum of Si contains weaker second-order features at 300 and 435 cm^{-1} [95] and, in some cases, these have led to their incorrect assignment as originating from the expected Ge–Ge and localized Si–Si modes in Ge dot nanostructures immersed in a Si matrix and grown on a Si substrate [108, 110]. These errors have arisen when the Raman spectra of the dots are relatively weak. There is a very simple solution to this problem, which has successfully been applied in the cases of weak scattering from $(Si_mGe_n)_p$ superlattices [143] and $Si_{1-x}C_x$ epitaxial layers [136]. The desired weak Raman features are revealed by a scaling (based on the strong Si line at 520 cm^{-1}) and

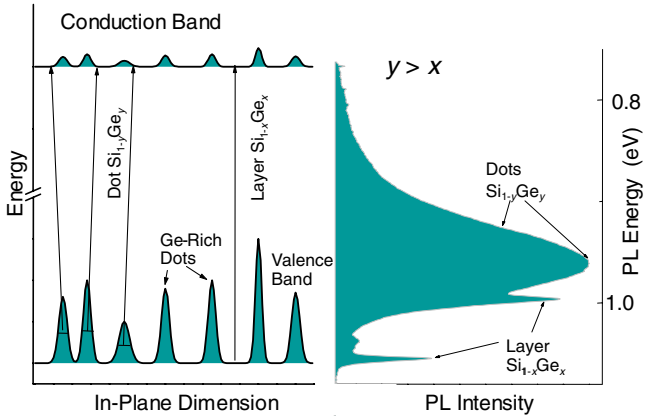

Figure 15. A schematic representation (left panel) of the energy band variations due to clustering and dot formation in a $Si_{1-x}Ge_x$ layer. The corresponding PL spectrum (right panel) exhibits dot related and layer recombination peaks.

subtraction process to remove the Si substrate and Si epitaxial layer contribution to the Raman spectrum.

3.6. Optical properties and use of $Si_{1-x}Ge_x$ for photon detection

The physical phenomena responsible for the photoluminescence (PL) spectra of Ge dot structures are illustrated in figure 15. The left-hand side of this figure shows a schematic cross-section within a $Si_{1-x}Ge_x$ layer in a direction perpendicular to the growth direction where a number of relatively Ge-rich dots are illustrated as valence band energy peaks with corresponding but much weaker features in the conduction band. In the PL experiment, the excitons created at low temperature are localized first in the $Si_{1-x}Ge_x$ layers after diffusing vertically. Thereafter, the excitons diffuse laterally and generally become trapped in the relatively Ge-rich $Si_{1-y}Ge_y$ dots before the recombination of electrons and holes occurs. As the Ge concentration is locally high in the dots, the emitted photon energy is smaller than that for PL from the laterally adjacent $Si_{1-x}Ge_x$. However, the dot photon energy is not as small as the energy difference between the valence band at the dot centre and the conduction band because of a blueshift due to hole confinement in three dimensions. The right panel of figure 15 indicates how this further localization perpendicular to the growth direction is manifested in a real PL spectrum in which the relatively narrow $Si_{1-x}Ge_x$ layer PL (consisting of the no-phonon (NP) line and its phonon replica) is superimposed on the Ge island PL to lower energy. This spectrum largely reflects the energy variations in the $Si_{1-x}Ge_x$ valence band, like that illustrated in the left panel of figure 15. The fact that the layer PL is observed along with the energetically favoured island recombination indicates the dots are relatively isolated since some excitons are being captured by the background impurities in the alloy layer before finding dots. Note that the island PL begins at an energy below the layer NP peak since the dots have a higher Ge concentration than the layers, which causes the recombination energy to have a significant net red shift (including confinement effects), the amount of which for a specific dot depends on its size and Ge concentration. Since there is a range of possible dot configurations, the spectrum for the sample ensemble of dots is necessarily much broader than the layer spectrum. In figure 16 we illustrate how the changeover from a 2D to a 3D growth mode influences the PL spectrum. The spectral change is quite remarkable, ranging

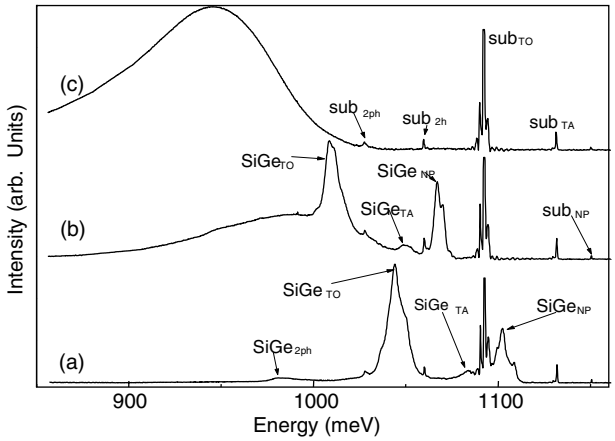

Figure 16. The evolution from phonon-resolved to dot PL demonstrated for three $Si/Si_{1-x}Ge_x$ superlattices of similar alloy composition but of different layer thicknesses. (a) 20 periods of (2.7 nm $Si_{0.85}Ge_{0.15}$/20 nm Si), (b) 20 periods of (5.2 nm $Si_{0.85}Ge_{0.15}$/20 nm Si), and (c) 15 periods of (6.8 nm $Si_{0.815}Ge_{0.185}$/30 nm Si).

from phonon-resolved (PR) (2D—lower trace) to dot (3D—upper trace) PL peaks for three superlattice structures grown by MBE at 600 °C. A similar behaviour has been observed in Ge growth by several authors where the growth mode changeover from 2D to 3D takes place at a specific Ge thickness [144]. In the present example, the superlattice growth sequences differed only in the $Si_{1-x}Ge_x$ alloy layer growth times, giving $Si_{1-x}Ge_x$ layer thicknesses of 2.7, 5.2, and 6.8 nm for samples (a), (b), and (c), respectively. In sample (a), the NP peaks originate from excitons in the 2.7 nm thick $Si_{0.85}Ge_{0.15}$ layers of the superlattice structure. In sample (b), an increase in the $Si_{0.85}Ge_{0.15}$ layer thickness to 5.2 nm reduces the confinement shift by 25 meV and a broad, dot-related PL peak is seen with its high energy edge near the PR NP energy. For sample (c), comprising $Si_{0.81}Ge_{0.19}$ layers 6.8 nm thick, PR PL is not observed and a more intense dot PL peak is seen shifted further down in energy. In the TEM diffraction contrast images of the three samples with PL spectra shown in figure 16, the density of Ge-rich dot islands increased markedly with $Si_{0.85}Ge_{0.15}$ layer thickness, mirroring the change in PL characteristics. This correlation was decisive in the assignment of the broad PL peak to self-annihilation of excitons within the Ge islands. In the transition from 2D to 3D PL, a decrease in the average TO phonon energy is expected, since, as the dots become more Ge-rich, the TO phonon energy will asymptotically tend towards the Ge–Ge value of 36 meV, well down from the Si–Si energy of 58 meV [145]. This variation contributes to the shape of the broad PL band, which contains unresolved, overlapped NP and TO bands. The leading edge of the overall PL band is relatively sharp compared with the trailing edge, because the three TO bands overlapped in the vicinity of the lower energy edge. It was observed that this low energy edge becomes sharpened as the Ge fraction in the dots increases and a single TO phonon (the Ge–Ge vibration) predominates. The PL band shape has been of great utility to many authors in order, for example, to obtain information regarding the dot size [146], shape [147], strain [148], uniformity [149], and internal Ge-fraction variation [150]. For example, the PL spectra in figure 17 for $Si_{1-y}Ge_y$ quantum dots self-organized within a $Si_{1-x}Ge_x$ layer show a narrowing on the lower frequency side as the background Ge fraction x increases, presumably because there is a commensurate increase in the peak Ge concentration in the dot. Since such an increase would favour the Ge–Ge TO phonon replica over the Si–Si TO, it would lead to

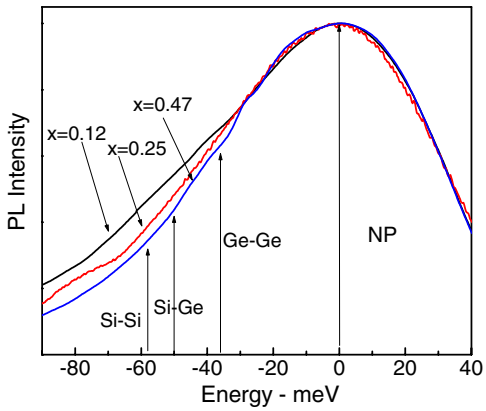

Figure 17. PL emission spectra for three samples containing self-organized SiGe quantum dots. The spectra have been energy shifted for their peaks to coincide. The positions of the TO phonon replicas are indicated by arrows.

a narrowing of the overall SiGe PL peak—composed mainly of NP and TO components—because Ge–Ge phonons have lower frequency. In figure 17 the PL peaks have all been shifted to 0 meV for the direct comparison of lineshapes among the three samples. What is apparent is that while the high energy PL edge has essentially the same shape for the three samples, the lower energy edge becomes increasingly sharper with Ge concentration [145].

The connection between strain density and the spectra of figure 16 is consistent with changes in growth morphology (interfacial roughening where the onset of 3D growth takes place) that acts to reduce the strain energy of the superlattice stack. Since the other variables have been maintained constant in this comparison, and only slight differences in Ge fraction exist between the superlattices, the strained layer thicknesses remain the only significant difference in the series. The build-up of strain energy results in metastable structures that become thermodynamically unstable with respect to relaxation during growth by several strain relief mechanisms. However, in these samples, no evidence from TEM for misfit dislocation, one important possible relaxation mechanism, was observed, even in the high strain energy density samples where only Ge dot PL was obtained. This indicates that strain accommodation occurs through morphological evolution and formation of Ge-rich regions. Since the build-up of strain energy density during growth is proportional to the square of the Ge fraction, increases linearly with each strained $Si_{1-x}Ge_x$-layer deposition, and remains constant during Si-layer growth, there are significant differences between the three superlattices of figure 16 regarding accumulated strain. From these samples and many others comprising a wide range of $Si/Si_{1-x}Ge_x$ multilayers [151], the strain energy contours that separate regimes of different PL behaviour—PR only, PR/dot, and dot—are fairly well established and indicate that the growth morphology transition occurs at a strain energy density near 10^5 J m^{-2}.

In none of the samples reported in the present work or in Rowell *et al* [151] were dislocation peaks seen in the PL spectra nor were significant dislocation densities present in the TEM images or XRD scans. Therefore the conclusions of work on relaxed material, for example, Hartmann *et al* [152], which formed the basis for the T-band hypothesis, would not seem to be relevant here. We also mention the fact that no energy gap was seen between the PLE and PL spectrum [151]. A gap would be present for the isoelectronic centre responsible for the T band. Furthermore, the total SiGe thickness in our samples is far less than that reported for the T band, e.g. as in [152] for $x = 0.12$.

As discussed earlier [151] and above, the transition from pure 2D growth to mixed 2D/3D growth occurs around a critical strain energy density, which increases during growth, quadratically with Ge fraction and linearly with SiGe thickness. Hence for a multiple-quantum-well structure of a given Ge fraction, it is expected that a critical density would be exceeded as the number of periods is increased, meaning that the initially grown wells would have 2D growth and the later ones a mixed 2D/3D growth. This phenomenon was explored in Rowell *et al* [151] where results of several experiments testing the hypothesis were presented, notably figure 17 of that reference in which the outer 2D/3D growth mode wells were etched off, effectively killing the 3D broad PL but leaving the 2D resolved PL intact. Certainly, the abrupt disappearance of the 3D PL band while the 2D PL band was still present was a very different basic behaviour to that observed for the T band by Hartmann *et al*, who said that the centres responsible for this band were uniformly distributed in the vertical direction. Our different result provides further confirmation that we are not observing the T band in the present material.

Dashiell *et al* [153] show that for RTA at 660 °C the 3D broad PL peak remains much the same except for a blueshift due to intermixing. However above 660 °C, the authors saw a transition to phonon-resolved (2D) peaks, separated in energy by 55 meV, which is slightly smaller than the normal value (58 meV), probably because the structure's SiGe material had an inhomogeneous Ge concentration which is relatively high locally. The transition from 3D to 2D PL spectra occurred as the dot's confinement potential was washed out. In that work the authors stated that the shift and transition were further proof that the PL was not associated with misfit dislocations and was not, therefore, the T band. Previously we had reported the same sort of behaviour with annealing for samples similar to those used in our present work (see [151], figure 20), providing further evidence that what we are observing is 3D PL and not T-band PL.

In figure 16 varying amounts of 2D and 3D PL can be seen, e.g. no PL from the 2D layer is seen in figure 16(c). In a mixed 2D/3D layer, whether or not one observes both 2D and 3D PL depends on the island density and the exciton diffusion length. The diffusion length decreases, for example, with the background impurity concentration. At higher island densities essentially all the excitons are captured by the islands since these are 3D potential wells for holes. In this case one observes the 3D broad peak exclusively. When the island density is low, excitons have larger probability of finding impurity atoms and recombining there when 2D (phonon-resolved) PL is observed. Of course at intermediate densities 3D and 2D PL can be observed simultaneously, when, as illustrated in our previous work, it is possible to vary these effects by changing parameters in the PL experiment, e.g. excitation wavelength, temperature, and excitation density [151].

Since among the samples of figure 16 neither the Ge fractions nor the layer thicknesses are identical, one should expect some variation in the PL spectrum for both the 2D and 3D peak positions. Clearly for 2D PL there is a blueshift associated with carrier confinement when SiGe layer thickness decreases and a redshift if the Ge fraction increases. Furthermore, the 3D PL depends strongly on the island size and peak 3D Ge concentration as well as on 2D parameters such as layer thickness and Ge fraction.

The broad-PL peak position for various MBE-grown $Si_{1-x}Ge_x$ stacked islands shifts to lower energy with increasing Ge content, as is shown in figure 18(a). Furthermore, for a given composition, the shift is less pronounced in samples with thinner alloy layers, indicating a confinement shift of the bandgap. The PL peak energy is below that of the bandgap energy for coherently strained $Si_{1-x}Ge_x$ alloy layers of the same composition, suggesting an increased concentration of Ge and a local strain relaxation at the apex of the island. Some quantum confinement shifts are also seen for undulating superlattices with a small (<4 nm) $Si_{1-x}Ge_x$ nominal layer thickness (see figure 18(a)). Figure 18(b) shows the typical PL time decay for

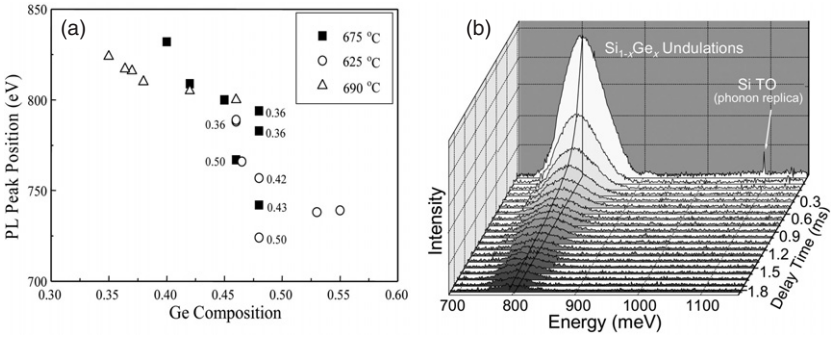

Figure 18. (a) PL peak position as a function of composition for various island superlattices grown by MBE at the temperature indicated. The number beside some data points is the nominal $Si_{1-x}Ge_x$ layer thickness (in nm) in the structure [16]. (b) Time decay of the PL signal at 5 K for a 3.3 nm thick $Si_{0.55}Ge_{0.045}$ 10 period structure grown at 675 °C.

MBE-grown $Si_{1-x}Ge_x$ stacked islands. The subsequent PL from the $Si_{1-x}Ge_x$ undulations decays towards lower photon energy with approximately a 200 μs time constant, in contrast to the PL from the underlying Si substrate, that decays much more rapidly. The PL is contained in a broad NP line with no resolved phonon replicas. The $Si_{1-x}Ge_x$ PL peak shifts to lower energy with increasing Ge fraction. The PL also moves to higher energy with increasing excitation density due to the fact that crests with highest Ge fraction (providing the lower energy PL) have an exciton accommodation limit, which leads to PL saturation for these crests. Hence, the PL from lower Ge-fraction crests predominates at higher excitation densities. At the same time, the PL from the higher Ge-fraction crests has a longer lifetime due to the tighter confinement of excitons in these regions. This longer lifetime is observed as the PL peak shifts to lower energy with increasing decay time. The decays for the phonon replica PL in the MBE material were found to be at least 100 times faster than for the dot PL. Although the result of figure 18(b) was obtained for self-organized island superlattices, similar decay lifetimes were observed for isolated islands.

The absorption edge of a $Si_{1-x}Ge_x$ quantum well can be extended to the telecommunication wavelength range and beyond, but the lowest lying transition is still indirect. As a result the optical absorption, and hence the carrier generation efficiency, remains small relative to direct gap materials. Planar $Si_{1-x}Ge_x$ alloys or pure Ge layers on Si were first used to extend the spectral response of photon detectors beyond the Si band-edge [154]. Although some progress has recently been reported [155], it is inherently difficult in standard 2D $Si_{1-x}Ge_x$ structures to reach telecommunication wavelengths because of the high Ge content needed to achieve the desired bandgap reductions. Nonetheless, the use of planar $Si_{1-x}Ge_x$ alloys has proven effective in fabricating photon detectors with reasonable quantum efficiencies at 1300 nm [156–158], but not at 1550 nm. In practice, Ge concentrations well over $x = 0.5$ are required to obtain a significant photocurrent response at 1550 nm, and the corresponding critical thicknesses of the order of 10 nm or less is unsuitable for device fabrication [19, 159]. In $Si_{1-x}Ge_x$ dots, the relaxation of the momentum conservation condition, as well as the 3D charge carrier confinement in the islands, is expected to significantly enhance the radiative recombination probability [160–163]. Vertical alignment in stacked layers of dots can also favour carrier transport through the structure and enhance radiative recombination. Electroluminescence, persisting to room temperature in some cases, has been reported in self-assembled stacked $Si_{1-x}Ge_x$ island diode structures [164–168]. The increasing importance of

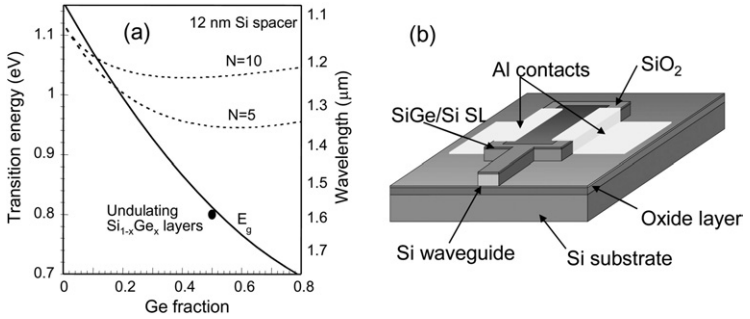

Figure 19. (a) Bandgap variation as a function of Ge fraction for coherently strained planar (dotted lines) and UHV-CVD grown undulated (full line) $Si/Si_{1-x}Ge_x$ superlattices with 12 nm thick Si spacer layers. (b) Schematic layout of an infrared photon detector based on an undulated $Si/Si_{1-x}Ge_x$ superlattice on a silicon-on-insulator substrate.

quantum confinement effects in such thin layers tends to push the absorption edge to shorter wavelengths, thus counteracting the effect of increasing the Ge concentration (see figure 19(a)). One solution has been to grow the $Si/Si_{1-x}Ge_x$ multilayers in a regime in which the interfaces are undulated rather than planar, with the waviness reducing the strain energy and allowing thicker layers. This 3D growth mode also increases the effective Ge concentrations where there are local maxima in the quantum well thickness, thus reducing the local quantum confinement at these locations. The 3D growth regime enables the growth of thermally robust and defect-free structures with high Ge content. Furthermore, the volume of active material may be increased through imbedding stacks of dot layers in thicker non-absorbing Si spacers or using a waveguide configuration to increase the absorption length [169, 170].

Undulated $Si_{1-x}Ge_x$ layers have been applied successfully in the fabrication of photon detectors operating at telecommunication wavelengths [16, 20, 171–175]. $Si_{1-x}Ge_x$ self-assembled islands imbedded in Si forming the intrinsic layer of a normal incidence p–i–n photon detector schematically illustrated in figure 19(b) have been shown to extend the photodetection range of these devices to 1.3 and 1.55 μm radiation with a room temperature responsivity of 0.2 and 0.003 A W^{-1} at these respective wavelengths [171]. It consists of stacked wavy $Si_{0.5}Ge_{0.5}$ layers grown by UHV-CVD on a silicon-on-insulator (SOI) substrate [176]. In this device, enhanced responsivity is obtained by increasing the active region by coupling radiation through a surface ridge waveguide [20]. Here, embedding $Si_{1-x}Ge_x$ layers in a SOI structure yields a well confined waveguide with the optical mode profiles mainly governed by the large index contrast between the Si and the oxide cladding. This wafer was fabricated into a waveguide metal–semiconductor–metal (MSM) photon detector with a geometry described elsewhere [176]. By placing the $Si_{1-x}Ge_x$ stack close to the surface and using inter-digitated electrodes at the surface, a responsivity of 0.1 A W^{-1} was demonstrated for $\lambda = 1.52$ μm [176]. As an alternative to the use of an SOI wafer, a thick dilute $Si_{1-x}Ge_x$ sub-layer has also been used to confine the optical modes in the active region of the detector [177]. This approach resulted in detectors of comparable responsivity at the telecommunication wavelengths to similar device structures grown on SOI wafers.

$Si/Si_{1-x}Ge_x$ island superlattice infrared photon detectors with fast response time have also been realized in a vertical metal/semiconductor/metal configuration by growing the active undulated superlattice by MBE on a Co silicide thin film epitaxially grown on (001) Si [175, 178, 179]. Here, electron–hole pairs are created in the small gap $Si_{1-x}Ge_x$ islands and the photocurrent is dominated by electrons drifting towards the silicide electrode. Detectors

with a response time of 12 ps and a quantum efficiency of 5 and 1% at 1.32 and 1.55 μm, respectively, have been reported [175]. Intra-valence band transitions in self-organized Ge dots can also be used to detect longer wavelength photons [180, 181]. Devices exhibiting a broad optical absorption in the wavelength range 2–6 μm with responsivities of several mA W^{-1} for 20 K operation were achieved with this approach.

4. Dot engineering

In order to exploit the unique properties of semiconductor quantum dots in novel devices, it is crucial to develop techniques to accurately control their size, density, and position. As outlined in the previous section, the simplest ways to tailor dots are thermal anneals, which cause a coarsening of the dots, and Si capping under various experimental conditions that can lead to changes in the shape and size. As the physical properties of Ge dots are now better understood, development of techniques to further engineer dot structures has recently become a very active axis of research. Beside intrinsic thermodynamics and kinetic constraints, other factors can influence dot formation. These can be classified into two categories, namely the factors that modify the substrate surface morphology and those that alter its physico-chemical properties. In the following we review recent progress in tailoring dot systems.

4.1. Dot control via surface morphology

Depositing dots on a substrate that possesses a particular intrinsic or extrinsic surface morphology is a straightforward way to tailor dot formation. For example, the presence of surface steps can influence the nucleation of Ge dots. It has been observed that Ge dots preferentially align at surface steps when grown on a vicinal (001) Si surface [182]. Si step bunching during growth of a Si buffer layer results in the formation of Ge dots in a transition region between (100) terraces and $\{11x\}$ facets, with $x = 8$–10. The lower coordination of Si atoms and concomitant partial lattice relaxation at steps both contribute to the preferential nucleation of Ge islands. Controlling accurately the miscut angle and orientation and devising ways to adjust the step height or terrace width may be a relatively easy way to control the placement of dots. This approach has recently been used successfully to produce ordered $Si_{1-x}Ge_x$ island structures on vicinal (001) Si [65, 66]. Surface undulations in $Si/Si_{1-x}Ge_x$ island superlattices may also represent a suitable template for the subsequent growth of ordered arrays of dots. Another way to exploit wafer misorientation is to deposit $Si_{1-x}Ge_x$ prior to the Ge dots. $Si_{1-x}Ge_x$ surface wires can be formed when an island superlattice is grown on a vicinal surface with a well oriented regular step distribution [183]. The surface waves have a period comparable to the size of the Ge dots and favour periodic arrangement of the dots. Ordered arrays of dots with surface symmetry governed by the direction of the substrate miscut have been achieved with this approach [184]. Besides dot positioning, this technique can offer some control of the dot size and prevent dot coalescence.

Island nucleation may be influenced by the strain field of a misfit dislocation network of a relaxed $Si_{1-x}Ge_x$ layer [185–189]. The misfit strain associated with these dislocations extends into the epitaxial layer and induces a regular variation in the lattice constant at the surface. This residual strain, albeit small, is sufficient to cause preferential nucleation of the Ge dots at the intersection of perpendicular misfit dislocations. This technique can in principle be used to control dot placement, but it may not be practical for most applications. This is because first the intrinsic random fluctuations in dislocation line spacing in relaxed epitaxial layers will result in a distribution of Ge islands on an irregular square grid and thus have limited accuracy on the positioning. Second, misfit dislocations are terminated by threading dislocations that may

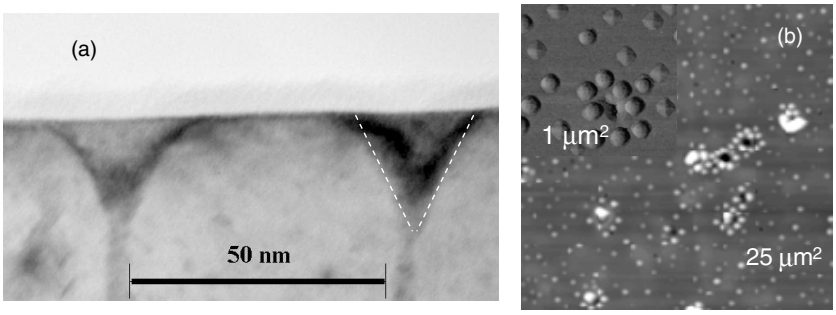

Figure 20. (a) Cross-sectional TEM view near the surface region of a homoepitaxial Si layer grown at 390 °C exhibiting a columnar growth and surface cusps. (b) AFM images of the surface morphology of a 6 ML Ge epitaxial layer grown by MBE on a Si epitaxial layer grown at 420 °C and exhibiting surface cusps.

propagate into the epitaxial films and in most cases adversely affect the optical and/or electrical properties of a device structure.

Other surface morphological features can promote dot nucleation. Surface pits, for example, may cause a high local surface step concentration or strain gradients suitable for dot formation. Dislocation-induced pits formed in relaxed island superlattices have been shown to act as preferential nucleation sites for Ge dots on (001) Si [190]. Surface cusps can also be observed in Si homo-epitaxy by MBE when growth is performed at a temperature close to that of epitaxy breakdown [191–193]. Figure 20(a) is a TEM cross-section view of the crystal structure of a 2 μm thick epitaxial Si film on (001) Si grown at 390 °C [194]. The surface exhibits a dense network of pits of ∼5–10 nm depth and 400 nm diameter. When Ge dots are grown on such a pitted surface, it is observed that nucleation is enhanced in the vicinity of surface pits. This is illustrated in figure 20(b), which displays an AFM image of Ge dots formed on a pitted Si surface. Here the Ge dots were obtained by depositing 6 ML of Ge at 650 °C on a (001) Si surface where pits were formed by pre-deposition of 2 μm of Si at a temperature of 420 °C. It is clear that the surface concentration of Ge dome islands is larger near surface pits and that, conversely, no pyramid dot is seen adjacent to the pits. The preferential nucleation and enhanced mass transport in the vicinity of the cusps may be associated with a local expansion of the Si lattice constant, as indicated by slight shift down in frequency of the Si Raman line, and is consistent with the results obtained when other types of intrinsic morphological features are present on the surface. This approach may be useful to control the relative numbers of pyramids and dome islands, but here again the randomness of the pit formation process makes it inadequate for accurate dot positioning.

The techniques outlined above can be applied quite easily, but offer limited control on the placement of dots. Lithography is another approach that can be used to etch a surface nano-template to control the size and exact placement of dots. Early attempts have exploited the high selectivity of chemical vapour deposition (CVD) to grow Si on Si stripes etched through a SiO_2 layer along the [100] direction [195]. This resulted in the formation of raised strips of epitaxial Si bounded by {011} side walls. This formed a template upon which Ge preferentially nucleated near the plateau edges forming a linear array of dots. Analogous results have been obtained on patterned Si with stripes along the [110] direction [196]. Here, the anisotropy of the growth rate leads to the formation of mesas of trapezoidal cross-section with {113} and {111} sidewall facets. Ge deposited on this surface resulted in a self-aligned well spaced 1D array of dots on the ridges of the mesas. Two-dimensional arrays of dots have also been obtained by growing on a surface patterned with square mesas. Si nano-imprinting at the 10–100 nm length scale

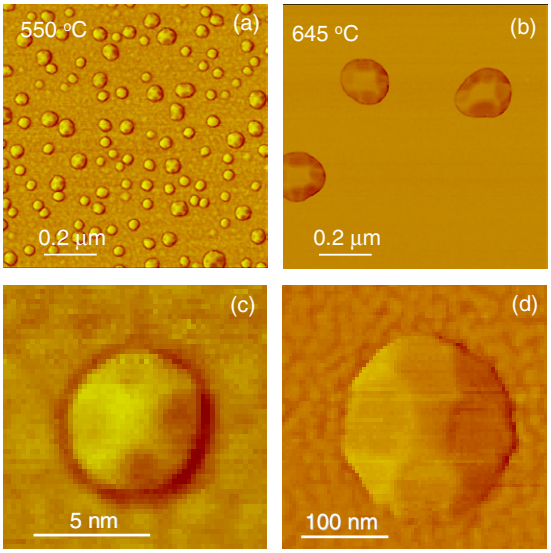

Figure 21. AFM images of the surface morphology of a series of ∼6 ML Ge epitaxial layers deposited by MBE. (a), (c) Growth at 550 °C on a surface pre-covered by ∼0.2 ML of C, (b) growth at 650 °C on a surface pre-covered with 0.2 ML C and (d) growth at 645 °C with ∼0.2 ML C inserted after deposition of 3 ML Ge [209, 210]. Note the difference between the island structure for the C pre-covered surface (b) and a similar structure grown without C, shown in figure 2(b).

has also been shown to be a good means to position Ge dots at a length scale difficult to attain by conventional lithography [197]. In all cases, preferential nucleation of dots at the ridges of stripe mesas likely results from a number of factors: higher adatom diffusion on the inclined sidewalls, a barrier to diffusion down the facets at the mesa edge and reduced strain energy at the edges. Similar results can be achieved via a non-selective growth technique such as MBE by depositing Si on a surface on which Si trenches have been etched [198–202]. Homo-epitaxy then results in an undulated morphology and offers preferred sites for dot nucleation [200]. In contrast with results obtained by CVD, the exact positioning of dots by MBE is more critically dependent on growth conditions and strain distribution. For example, on such an undulated surface, preferential nucleation of dots can occur at the sidewalls rather than on the top of the flat-top terraces. Nucleation at the top of the ridges may be achieved, however, if the surface is strained by the insertion of a $Si_{1-x}Ge_x$ buffer layer or if the growth temperature is increased [198, 199]. The interplay between surface kinetics, strain energy, and surface free energy is clearly crucial in determining the precise morphology. The mechanisms leading to dot alignment on topographically textured surfaces, and in particular the influence of deposition rate, have recently been discussed elsewhere [203].

4.2. Dot control via surface chemistry

While the presence of periodic morphological features on the surface greatly influences the placement and arrangement of Ge dots, it has relatively minor effects on their shape or physical dimensions. A modification of the surface chemistry through, for example, adsorption of foreign species, presence of a surfactant or dopant segregation may impact on the intrinsic properties of the dots. For example, the effect of carbon pre-treatment on the nucleation and evolution of Ge dots is a well studied example of dot engineering for the $Si_{1-x}Ge_x$ semiconductor system. The pre-deposition of a fraction of a monolayer of C on (001) Si

creates an inhomogeneous $Si_{1-x}C_x$ layer that strongly influences dot formation [204–212]. This is illustrated in figure 21, which compares MBE grown Ge dots formed with and without C pre-deposition at two different temperatures. At a low temperature of 550 °C and after pre-deposition of 0.2 ML C (figure 21(a)), deposition of ∼6 ML Ge results in the formation of a high density of dots. The dots are much smaller than normally seen on the Ge(001) Si system and exhibit a dome-like morphology. In comparison, Ge deposited in those conditions without the presence of C resulted in the formation of hut clusters [11]. Interestingly, the small domes have a very similar facet structure, as can be seen by comparison with the dome dot of figure 21(d) grown at high temperature. This result shows that C pre-treatment may be a practical means to tailor the size of dome-like Ge islands on (001) Si. The observation of a well established dot structure at low Ge coverage when C is pre-deposited is consistent with a thickness reduction or perhaps complete suppression of the Ge wetting layer in the presence of C [213]. Figure 21(b) shows the surface topography of a dot structure obtained at 650 °C by depositing 6 ML of Ge on (001) Si pre-covered by 0.2 ML carbon. Here only large dome islands are seen, while without C treatment a mixed distribution of pyramids and domes such as those shown in figure 2(b) is normally seen. In this case strain effects produced by C surface clusters may repel Ge adatoms, promoting the nucleation of larger Ge dots at a lower coverage [213].

The above examples illustrate how carbon pre-treatment makes it possible to synthesize dome-shaped Ge dots at low temperature and tailor their size and density through optimization of the growth conditions [208]. The size reduction of the domes puts them in a regime where quantum size effects are more prominent and possibly of interest for the conception of quantum optoelectronic devices. Ge dots prepared on (001) Si pre-covered with C have been shown to exhibit stronger low temperature luminescence properties as compared to dots prepared by conventional self-assembly [208, 214–218]. In this system, the luminescence arises from a spatially indirect recombination of electrons in the thin SiGeC wetting layer with holes within the Ge dots. A strong confinement shift in these small dots, however, results in a low activation energy and a quenching of the luminescence at 50 K, limiting the possibilities for applications [218].

Furthermore, the dot position is also strongly influenced by the distribution of surface carbon clusters and the vertical self-organization in stacked dot structures is lost in C mediated growth of dots [218], which may also be detrimental in applications. The actual physical mechanism that underlies the influence of C atoms on Ge dot formation is not fully elucidated and still a matter under debate.

Gas adsorption can influence dot formation. Atomic hydrogen acts as a surfactant in the Ge/(001) Si system, increasing the thickness of the wetting layer [219, 220]. The presence of H on the surface should have an opposing effect to C and retard the transition to 3D growth. Atomic hydrogen, by reducing Ge surface segregation and affecting surface diffusion, should also modify the structural properties of dots. Although the effect of atomic hydrogen on dot formation has not been studied in any detail, molecular hydrogen present in low pressure CVD growth has been found to shift the bimodal distribution of pyramids and domes to smaller sizes [207]. The use of Sb as a surfactant has also been found to influence the size and density of Ge dots [221, 222].

The introduction of dopants during growth may also influence dot formation by modifying the surface energy, by atomic bulk and surface diffusion or by blocking nucleation sites. For example, Sb-doped dome-shaped Ge islands have been observed to develop large {100} facets upon annealing, while In-doped Ge islands exhibited strong faceting upon annealing [223]. More recently [224], P doping was found to have a stabilizing effect on dome islands and to inhibit coarsening upon annealing. Finally, insertion of a sub-monolayer of boron on the Ge wetting layer can influence the subsequent growth of Ge, promoting the nucleation of small

dots at low coverage through strain effects and slowing down the dot evolution at high coverage through strain compensation by interdiffusion [225].

All of the above examples illustrate the broad possibilities that are offered to tailor dot fabrication. Because of its high level of control and reproducibility, growth on patterned substrates is certainly the most promising direction to achieve device compatible structures. Research on chemical treatment of surfaces should not be neglected, however, as if used in conjunction with patterning techniques it may lead to further optimization of tailored quantum dot structures.

5. Conclusion

In this paper, we have reviewed recent advances in the research on self-assembled Ge dots and $Si_{1-x}Ge_x$ islands. The principal points to emphasize are as follows.

- Island and dot formation in the Si–Ge system results from the interplay between the surface free energy and the built-in strain energy. Minimization of energy and kinetic barriers dictates the evolution of the epitaxial film morphology.
- Stacked layers of dots or islands in the form of superlattices are strongly correlated vertically. Island superlattices possess a characteristic modulation length that is a function of the strain and elastic properties of the material.
- The photoluminescence signature of $Si_{1-x}Ge_x$ islands is a broad peak at about 800 meV. The exact energy, breadth, and intensity of the PL signal all depend on physical properties such as the dimension of the islands, their size distribution, average composition, and strain.
- $Si_{1-x}Ge_x$ dot growth can be engineered either through semiconductor surface treatment or surface patterning.

Originally perceived as undesirable three-dimensional features, self-assembled dots are now amongst the most studied semiconductor hetero-epitaxial systems. In the case of the Ge/(001) Si system, now that dot formation is better understood and their physical properties are becoming elucidated, the emphasis is shifting toward the exploitation of these nanostructures in novel devices. In particular, SiGe nanostructures represent possible building blocks for 'applied quantum mechanics' [226], where devices exploit fundamental quantum principles. Of critical importance will be to perfect techniques to accurately control the physical parameters and the placement of dots, and to devise ways to incorporate them in actual device geometries. Progress is already being made in the production of well regimented dots on top of pyramids or mesas to form the 0D structures and 1D or 2D arrays needed in many applications [190, 227]. The possibility to exploit morphological instabilities such as found in island superlattices to tailor surfaces at the nanometre scale also opens up interesting directions. Surfaces exhibiting a regular corrugation and strain distribution at a well defined length scale such as those depicted in figure 7 may be of interest for sensor applications through surface functionalization. In analogy with the development of strained Si for high speed electronics, further research on strain engineering in the Si/Ge system is anticipated. For example, further control of dot morphology and physical properties may be achieved by growth on compliant substrates [228, 229]. The synthesis of island superlattices on alternative substrates such as silicon-on-insulator [230] or silicide thin films [175, 178, 179] is also a promising direction. Despite all the challenges that remain in the understanding and control of semiconductor nanostructures, these artificial materials constitute a key enabling technology leading to the development of quantum devices and eventually quantum computing.

Acknowledgments

We wish to express our thanks to the many co-workers and collaborators who have contributed over the years to the growth and study of $Si_{1-x}Ge_x$ dots and islands at the National Research Council.

References

[1] Ishimaru N, Ueba H and Tatsuyama C 1988 *Surf. Sci.* **193** 193
[2] Tatsuyama C, Ueba H and Kataoka Y 1988 *Appl. Surf. Sci.* **33/34** 457
[3] Swanson M L, Parikh N R, Frey E C, Sandhu G S, Chu W K, Jackman T E, Baribeau J-M, Kechang S and McCaffrey J 1989 *Characterization of the Structure and Chemistry of Defects in Materials* ed B C Larson, M Rühle and D N Seidman (Boston, MA: Materials Research Society) p 581
[4] Eaglesham D J and Cerullo M 1990 *Phys. Rev. Lett.* **64** 1943
[5] Mo Y-W, Savage D E, Swartzentruber B S and Lagally M G 1990 *Phys. Rev. Lett.* **65** 1020
[6] Asaro R J and Tiller W A 1972 *Metall. Trans.* A **3** 1789
[7] Grinfeld M A 1986 *Dokl. Akad. Nauk SSSR* **290** 1358
[8] Teichert B 2002 *Phys. Rep.* **365** 335
[9] Zhang Z and Lagally M G (ed) 1998 *Morphological Organization in Epitaxial Growth and Removal* (Singapore: World Scientific) p 498
[10] Brunner K 2002 *Rep. Prog. Phys.* **65** 27
[11] Baribeau J-M, Rowell N L and Lockwood D J 2006 *Self-Organized Nanoscale Materials* ed M Adachi and D J Lockwood (New York: Springer) p 1
[12] Stangl A, Holý V and Bauer G 2004 *Rev. Mod. Phys.* **76** 725
[13] Baribeau J M, Jackman T E, Houghton D C, Maigné P and Denhoff M W 1988 *J. Appl. Phys.* **63** 5738
[14] Baribeau J-M 1995 *J. Cryst. Growth* **157** 52
[15] Baribeau J-M, Houghton D C, Jackman T E and McCaffrey J P 1989 *J. Electrochem. Soc.* **136** 1158
[16] Baribeau J-M, Delâge A, Janz S, Lafontaine H, Lockwood D J, McCaffrey J P, Moisa S, Rowell N L and Xu D-X 1999 *Advanced Luminescent Materials and Quantum Confinement* ed M Cahay, S Bandyopadhyay, D J Lockwood, J P Leburton, N Koshida, M Meyyappan and T Sakamoto (Pennington: The Electrochemical Society) p 45
[17] Baribeau J-M, Lockwood D J, Dharma-wardana M W C, Rowell N L and McCaffrey J P 1989 *Thin Solid Films* **183** 17
[18] Lafontaine H, Houghton D C, Elliott D, Rowell N L, Baribeau J-M, Laframboise S, Sproule G I and Rolfe S J 1996 *J. Vac. Sci. Technol.* B **14** 1675
[19] Lafontaine H, Houghton D C, Bahierathan B, Perovic D D and Baribeau J-M 1999 *Evolution of Expitaxial Structure and Morphology* ed A Zangwill, D Jesson, D Chambliss and R Clarke (Pittsburg, PA: Materials Research Society) p 413
[20] Lafontaine H, Rowell N L, Janz S and Xu D-X 1999 *J. Appl. Phys.* **86** 1287
[21] Baribeau J-M, Jackman T E, Houghton D C, Maigné P and Denhoff M W 1988 *J. Appl. Phys.* **63** 5738
[22] Baribeau J-M and Lafontaine H 1998 *Thin Solid Films* **321** 141
[23] Baribeau J-M 1998 *J. Vac. Sci. Technol.* B **16** 1568
[24] Baribeau J-M 1988 *Appl. Phys. Lett.* **52** 105
[25] Lockwood D J, Dharma-wardana M W C, Baribeau J-M and Houghton D C 1987 *Phys. Rev.* B **35** 3243
[26] Jain S C 1994 *Germanium–Silicon Strained Layers and Heterostructures* (Boston, MA: Academic)
[27] Stranski I N and Krastanow L 1937 *Sitz. ber, Akad. Wien, Mater. Nat. K1.* IIb **146** 797
[28] Vailionis A, Cho B, Glass G, Desjardins P, Cahill D G and Greene J E 2000 *Phys. Rev. Lett.* **85** 3672–5
[29] Ross F M, Tromp R M and Reuter M C 1999 *Science* **286** 1931
[30] Tersoff J and LeGoues F K 1994 *Phys. Rev. Lett.* **72** 3570
[31] Shchukin V A, Ledentsov N N, Kop'ev P S and Bimberg D 1995 *Phys. Rev. Lett.* **75** 2968
[32] Shklyaev O E, Beck M J, Asta M, Miksis M J and Voorhees P W 2005 *Phys. Rev. Lett.* **94** 176102
[33] Lu G-H and Liu F 2005 *Phys. Rev. Lett.* **94** 176103
[34] Daruka I, Tersoff J and Barabási A-L 1999 *Phys. Rev. Lett.* **82** 2753
[35] Costantini G, Rastelli A, Manzano C, Songmuang R, Schmidt O G, Kern K and Känel H v 2004 *Appl. Phys. Lett.* **85** 5673
[36] Costantini G, Rastelli A, Manzano C, Acosta-Diaz P, Katsaros G, Songmuang R, Schmidt O G, Kanel H v and Kern K 2005 *J. Cryst. Growth* **278** 38

[37] Chaparro S A, Zhang Y, Drucker J, Chandrasekhar D and Smith D J 2000 *J. Appl. Phys.* **87** 245
[38] Drucker J and Chapparo S 1997 *Appl. Phys. Lett.* **71** 614
[39] Seta M D, Capellini G, Evangelisti F and Spinella C 2002 *J. Appl. Phys.* **92** 614
[40] Zhang Y and Drucker J 2003 *J. Appl. Phys.* **93** 9583
[41] Floro J A, Sinclair M B, Chason E, Freund L B, Twesten R D, Hwang R Q and Lucadamo G A 2000 *Phys. Rev. Lett.* **84** 701
[42] Liu P, Zhang Y W and Lu C 2003 *Phys. Rev.* B **68** 035402
[43] Kamins T I, Medeiros-Ribeiro G, Ohlberg D A A and Williams R S 1999 *J. Appl. Phys.* **85** 1159
[44] Cho B, Schwarz-Selinger T, Ohmori K, Cahill D G and Greene J E 2002 *Phys. Rev.* B **66** 195407
[45] Capellini G, De Seta M and Evangelisti F 2002 *Mater. Sci. Eng.* B **89** 184
[46] Rastelli A, Kummer M and Känel H v 2001 *Phys. Rev. Lett.* **87** 256101
[47] Rastelli A, Muller E and Känel H v 2002 *Appl. Phys. Lett.* **80** 1438
[48] Loo R, Meunier-Beillard P, Vanhaeren D, Bender H, Caymax M, Vandervorst W, Dentel D, Goryll M and Vescan L 2001 *J. Appl. Phys.* **90** 2565
[49] Liu J P, Wang J Z, Huang D D, Li J P, Sun D Z and Kong M Y 1999 *J. Cryst. Growth* **207** 150
[50] Sutter P and Lagally M G 1998 *Phys. Rev. Lett.* **81** 3471
[51] Floro J A, Chason E, Twesten R D, Hwang R Q and Freund L B 1997 *Phys. Rev. Lett.* **79** 3946–9
[52] Walther T, Cullis A G, Norris D J and Hopkinson M 2001 *Phys. Rev. Lett.* **86** 2381
[53] Cullis A G, Norris D J, Walther T, Migliorato M A and Hopkinson M 2002 *Phys. Rev.* B **66** 081305
[54] Tu Y and Tersoff J 2004 *Phys. Rev. Lett.* **93** 216101
[55] Ginley R A, Chung D D L and Ginley D S 1984 *Solid-State Electron.* **27** 137
[56] Gao H 1994 *J. Mech. Phys. Solids* **42** 741
[57] Tu K-N, Mayer J W and Feldman L C 1992 *Electronic Thin Film Science for Electrical Engineers and Materials Scientists Appendix E* (New York: Macmillan)
[58] Springholz G 2005 *C. R. Phys.* **6** 89
[59] Schmidt O G, Jin-Phillipp N Y, Lange C, Denker U, Eberl K, Schreiner R, Grabeldinger H and Schweizer H 2000 *Appl. Phys. Lett.* **77** 4139
[60] Stangl J, Roch T, Bauer G, Kegel I, Metzger T H, Schmidt O G, Eberl K, Kienzle O and Ernst F 2000 *Appl. Phys. Lett.* **77** 3953
[61] Le Thanh V and Yam V 2003 *Appl. Surf. Sci.* **212/213** 296
[62] Tersoff J, Teichert C and Lagally M G 1996 *Phys. Rev. Lett.* **76** 1675
[63] Sutter E, Sutter P and Vescan L 2002 *Mater. Sci. Eng.* B **89** 196
[64] Silvestre C, Jernigan G G, Twigg M E and Thompson P E 1998 *J. Vac. Sci. Technol.* B **16** 1933
[65] Lichtenberger H, Muhlberger M and Schäffler F 2005 *Appl. Phys. Lett.* **86** 131919
[66] Lichtenberger H, Muhlberger M, Schelling C and Schäffler F 2005 *J. Cryst. Growth* **278** 78
[67] Brunner K, Zhu J, Miesner C, Abstreiter G, Kienzle O and Ernst F 2000 *Physica* E **7** 881
[68] Cullis A G, Robbins D J, Barnett S J and Pidduck A J 1994 *J. Vac. Sci. Technol.* A **12** 1924
[69] Stangl J, Daniel A, Holý V, Roch T, Bauer G, Kegel I, Metzger T H, Wiebach T, Schmidt O G and Eberl K 2001 *Appl. Phys. Lett.* **79** 1474
[70] Hesse A, Stangl J, Holý V, Roch T, Bauer G, Schmidt O G, Denker U and Struth B 2002 *Phys. Rev.* B **66** 085321
[71] Schülli T U, Stangl J, Zhong Z, Lechner R T, Sztucki M, Metzger T H and Bauer G 2003 *Phys. Rev. Lett.* **90** 066105
[72] Magalhaes-Paniago R, Medeiros-Ribeiro G, Malachias A, Kycia S, Kamins T I and Williams R S 2002 *Phys. Rev.* B **66** 245312/1
[73] Malachias A, Kycia S, Medeiros-Ribeiro G, Magalhaes-Paniago R, Kamins T I and Williams R S 2003 *Phys. Rev. Lett.* **91** 176101
[74] Schmidt O G and Eberl K 2000 *Phys. Rev.* B **61** 13721–9
[75] Schmidt O G, Denker U, Christiansen S and Ernst F 2002 *Appl. Phys. Lett.* **81** 2614
[76] Zhi D, Wei M, Pashley D W, Joyce B A, Weyland M, Laffont L, Yates T J V, Twitchett A C, Dunin-Borkowski R E and Midgley P A 2004 *Electron Microscopy and Analysis 2003* ed S McVitie and D McComb (Oxford: Institute of Physics Publishing) p 39
[77] Lang C, Nguyen-Manh D and Cockayne D J H 2004 *EMAG2003: Electron Microscopy and Analysis Group Conference* ed S McVitie and D McComb (Oxford: Institute of Physics Publishing) p 35
[78] Yates T J V, Laffont L, Zhi D and Midgley P A 2004 *EMAG2003: Electron Microscopy and Analysis Group Conference* ed S McVitie and D McComb (Oxford: Institute of Physics Publishing) p 31

[79] Zhi D, Midgley P A, Dunin-Borkowski R E, Joyce B, Pashley D W, Bleloch A L and Goodhew P J 2005 *Group-IV Semiconductor Nanostructures* ed L Tsybeskov, D J Lockwood, C Delerue and M Ichikawa (Pittsburgh, PA: Materials Research Socitey) p F5.4.1
[80] Miller P D, Liu C-P and Murray Gibson J 2000 *Ultramicroscopy* **84** 225
[81] Liu C-P, Twesten R D and Gibson J M 2000 *Ultramicroscopy* **87** 79
[82] Baribeau J-M, Wu X and Lockwood D J 2005 *J. Vac. Sci. Technol.* B at press
[83] Smith D J, Chandrasekhar D, Chaparro S A, Crozier P A, Drucker J, Floyd M, McCartney M R and Zhang Y 2003 *J. Cryst. Growth* **259** 232
[84] Fukatsu S, Fujita K, Yaguchi H, Shiraki Y and Ito R 1991 *Appl. Phys. Lett.* **59** 2103
[85] Ohta G, Fukatsu S, Ebuchi Y, Hattori T, Usami N and Shiraki Y 1994 *Appl. Phys. Lett.* **65** 2975
[86] Liu C P, Gibson J M, Cahill D G, Kamins T I, Basile D P and Williams R S 2000 *Phys. Rev. Lett.* **84** 1958
[87] Neumann W, Kirmse H, Hausler I, Otto R and Hahnert I 2004 *J. Alloys Compounds* **382** 2
[88] Chen Y and Washburn J 1996 *Phys. Rev. Lett.* **77**
[89] Ide T, Sakai A and Shimizu K 1999 *Thin Solid Films* **357** 22
[90] Raiteri P, Miglio L, Valentinotti F and Celino M 2002 *Appl. Phys. Lett.* **80** 3736
[91] Huang C J, Zuo Y H, Li D Z, Cheng B W, Luo L P, Yu J Z and Wang Q M 2001 *Appl. Phys. Lett.* **78** 3881
[92] Denker U, Schmidt O G, Jin-Philipp N-Y and Eberl K 2001 *Appl. Phys. Lett.* **78** 3723
[93] Liao X Z, Zou J, Cockayne D J H, Qin J, Jiang Z M, Wang X and Leon R 1999 *Phys. Rev.* B **60** 15605
[94] Sonnet P and Kelires P C 2004 *Appl. Phys. Lett.* **85** 203
[95] Menéndez J 2000 *Raman Scattering in Materials Science* ed W H Weber and R Merlin (Berlin: Springer) p 55
[96] Wasilewski Z R, Dion M M, Lockwood D J, Poole P, Streater R W and SpringThorpe A J 1997 *J. Appl. Phys.* **81** 1883
[97] Lockwood D J, Radomski R and Wasilewski Z R 2002 *J. Raman Spectrosc.* **33** 202
[98] Ruf T 1998 *Phonon Raman Scattering in Semiconductors, Quantum Wells and Superlattices* (Berlin: Springer)
[99] Shin H K, Lockwood D J and Baribeau J-M 2000 *Solid State Commun.* **114** 505
[100] Tang Y S, Sotomayer Torres C M, Dietrich B, Kessinger W, Whall T E and Parker E H C 1995 *Solid State Commun.* **94** 369
[101] Talochkin A B, Markov V A, Suprun S P and Nikiforov A I 1996 *JETP Lett.* **64** 219
[102] Wang X, Jiang Z-M, Zhu H J, Huang D, Liu X, Hu C W, Chen Y, Zhu Z and Yao T 1997 *Appl. Phys. Lett.* **71** 3543
[103] Darhuber A A, Grill T, Stangl A, Bauer G, Lockwood D J, Noël J-P, Wang P D and Sotomayer Torres C M 1998 *Phys. Rev.* B **58** 4825
[104] Kwok S H, Yu P Y, Tung C H, Zhang Y H, Li M F, Peng C S and Zhou J M 1999 *Phys. Rev.* B **59** 4980
[105] Liu J L, Tang Y S, Wang K L, Radetic T and Gronsky R 1999 *Appl. Phys. Lett.* **74** 1863
[106] Talochkin A B, Markov V A, Nikiforov A I and Tiis S A 1999 *JETP Lett.* **70** 288
[107] Zhu J H, Meisner C, Brunner K and Abstreiter G 1999 *Appl. Phys. Lett.* **75** 2395
[108] Kolobov A V and Tanaka K 1999 *Appl. Phys. Lett.* **75** 3572
[109] Liu J L, Jin G, Tang Y S, Luo Y H, Wang K L and Yu D P 2000 *Appl. Phys. Lett.* **76** 586
[110] Kolobov A V 2000 *J. Appl. Phys.* **87** 2926
[111] Liu J L, Jin G, Tang Y S, Luo Y H, Wang K L and Yu D P 2000 *J. Electron. Mater.* **29** 554
[112] Milekhin A, Stepina N P, Yakimov A I, Schulze S and Zahn D R T 2000 *Eur. Phys. J.* B **16** 355
[113] Yu P Y 2001 *Appl. Phys. Lett.* **78** 1160
[114] Guedj C, Beyer A, Müller E and Grützmacher D 2001 *Appl. Phys. Lett.* **78** 1742
[115] Milekhin A, Stepina N P, Yakimov A I, Nikiforov A I, Schulze S and Zahn D R T 2001 *Appl. Surf. Sci.* **175/176** 629
[116] Cazayous M, Groenen J, Huntzinger J R, Mlayah A and Schmidt O G 2001 *Phys. Rev.* B **64** 033306
[117] Milekhin A G, Nikiforov A I, Pchelyakov O P, Schulze S and Zahn D R T 2001 *JETP Lett.* **73** 461
[118] Wan J, Luo Y H, Jiang Z M, Jin G, Liu J L, Liao X Z, Wang K L and Zou J 2001 *J. Appl. Phys.* **90** 4290
[119] Milekhin A G, Nikiforov A I, Pchelyakov O P, Schulze S and Zahn D R T 2002 *Physica* E **13** 982
[120] Kolobov A V, Oyanagi H, Brunner K, Abstreiter G, Maeda Y, Shklyaev A A, Yamasaki S, Ichikawa M and Tanaka K 2002 *J. Vac. Sci. Technol.* A **20** 1116
[121] Kolobov A V, Morita K, Itoh K M and Haller E E 2002 *Appl. Phys. Lett.* **81** 3855
[122] Ren S-F and Cheng W 2002 *Phys. Rev.* B **66** 205328
[123] Liu J L, Wan J, Jiang Z M, Khitun A, Wang K L and Yu D P 2002 *J. Appl. Phys.* **92** 6804
[124] Darma Y, Murakami H and Miyazaki S 2003 *Japan. J. Appl. Phys.* **42** 4129
[125] Tan P H, Brunner K, Bougeard D and Abstreiter G 2003 *Phys. Rev.* B **68** 125302/1
[126] Kamenev B V, Grebel H, Tsybeskov L, Kamins T I, Williams R S, Baribeau J M and Lockwood D J 2003 *Appl. Phys. Lett.* **83** 5035

[127] Kamenev B V, Tsybeskov L, Baribeau J-M and Lockwood D J 2004 *Appl. Phys. Lett.* **84** 1293
[128] Yang Z, Shi Y, Yan B, Huang Z X, Pu L, Zheng Y D and Wang K L 2003 *Chin. Phys. Lett.* **20** 2001
[129] Rzaev M M, Burbaev T M, Kurbatov V A, Melnik N N, Muhlberger M, Pogosov A O, Schäffler F, Sibeldin N N, Tsvetkov V A, Werner P, Zakharov N D and Zavaritskaya T N 2003 *Phys. Status Solidi* c **4** 1262
[130] Talochkin A B and Teys S A 2002 *JETP Lett.* **75** 264
[131] Teo K L, Shen Z X and Schmidt O G 2004 *Phys. Status Solidi* b **241** 3274
[132] Valakh M Y *et al* 2005 *Phys. Solid State* **47** 54
[133] Milekhin A G, Nikiforov A I, Ladanov M Y, Pchelyakov O P, Schulze S and and Zahn D R T 2004 *Phys. Solid State* **46** 92
[134] Dzhagan V N, Krasil'nik Z F, Lytvyn P M, Novikov A V, Valakh M Y and Yukhymchuk V O 2003 *Semicond. Phys. Quantum Electron. Optoelectron.* **6** 164
[135] Milekhin A G, Nikiforov A I, Pchelyakov O P, Rodrigues A G, Galzerani J C and Zahn D R T 2005 *JETP Lett.* **81** 30
[136] Lockwood D J, Xu H X and Baribeau J-M 2003 *Phys. Rev.* B **68** 115308
[137] Lockwood D J and Baribeau J-M 1992 *Phys. Rev.* B **45** 8565
[138] Baribeau J-M and Lockwood D J 1992 *Thin Films, Stresses and Mechanical Properties III* ed W D Nix, J C Bravman, E Artz and L B Freund (Boston, MA: Materials Research Society) p 449
[139] Dismukes J P, Ekstrom L and Paff R J 1964 *J. Phys. Chem.* **68** 3021
[140] Fuchs H D, Grein C H, Alonso M I and Cardona M 1991 *Phys. Rev.* B **44** 13120
[141] Dharma-wardana M W C, Aers G C, Lockwood D J and Baribeau J-M 1990 *Phys. Rev.* B **41** 5319
[142] Tan P H, Bougeard D, Abstreiter G and Brunner K 2004 *Appl. Phys. Lett.* **84** 2632
[143] Lockwood D J, Baribeau J-M, Jackman T E, Aebi P, Tyliszczak T, Hitchcock A P and Headrick R L 1993 *Scanning Microsc.* **7** 457
[144] Schmidt O G, Lange C and Eberl K 1999 *Phys. Status Solidi* b **215** 319
[145] Rokhinson L P, Tsui D C, Benton J L and Xie Y-H 1999 *Appl. Phys. Lett.* **75** 2413
[146] Lobanov D N, Novikov A V, Vostokov N V, Drozdov Y N, Yablonskiy A N, Krasilnik Z F, Stoffel M, Denker U and Schmidt O G 2005 *Opt. Mater.* **27** 818
[147] Stoffel M, Kar G S, Denker U, Rastelli A, Sigg H and Schmidt O G 2004 *Physica* E **23** 421
[148] Martinelli L, Marzegalli A, Raiteri P, Bollani M, Montalenti F, Miglio L, Chrastina D, Isella G and Känel H v 2004 *Appl. Phys. Lett.* **84** 2895
[149] Chen P S, Lee S W, Peng Y H, Liu C W and Tsai M J 2004 *Phys. Status Solidi* b **241** 3650
[150] Vostokov N V, Krasil'nik Z F, Lobanov D N, Novikov A V, Shaleev M V and Yablonsky A N 2005 *Phys. Solid State* **47** 38
[151] Rowell N L, Noël J-P, Houghton D C, Wang A, Lenchyshyn L C, Thewalt M L W and Perovic D D 1993 *J. Appl. Phys.* **74** 2790
[152] Hartmann A, Vescan L, Dieker C, Stoica T and Lüth H 1993 *Phys. Rev.* B **48** 18276
[153] Dashiell M W, Denker U, Muller C, Costantini G, Manzano C, Kern K and Schmidt O G 2002 *Appl. Phys. Lett.* **80** 1279
[154] Luryi S, Kastalsky A and Bean J C 1984 *IEEE Trans. Electron Devices* **31** 1135
[155] Fama S, Colace L, Masini G and Assanto G 2002 *Appl. Phys. Lett.* **81** 586
[156] Temkin H, Pearsall T P, Bean J C, Logan R A and Luryi S 1986 *Appl. Phys. Lett.* **48** 963
[157] Splett A, Zinke T, Petermann K, Kasper E, Kibbel H, Herzog H-J and Presting H 1994 *Photon. Technol. Lett. IEEE* **6** 59
[158] Samavedam S B, Currie M T, Langdo T A and Fitzgerald E A 1998 *Appl. Phys. Lett.* **73** 2125
[159] Houghton D C 1991 *J. Appl. Phys.* **70** 2136
[160] Tang Y S, Ni W-X, Sotomayer Torres C M and Hansson G V 1995 *Electron. Lett.* **31** 1385
[161] Tsybeskov L and Lockwood D J 2000 *Asian J. Phys.* **9** 745
[162] Tsybeskov L, Hirschman K D, Duttagupta S P, Zacharias M, Fauchet P M, McCaffrey J P and Lockwood D J 1998 *Appl. Phys. Lett.* **72** 43
[163] Lockwood D J 2001 *Silicon-Based Materials and Devices* ed H S Nalwa (New York: Academic) p 225
[164] Apetz R, Vescan L, Hartmann A, Dieker C and Lüth H 1995 *Appl. Phys. Lett.* **66** 445
[165] Brunhes T, Boucaud P, Sauvage S, Aniel F, Lourtioz J-M, Hernandez C, Campidelli Y, Kermarrec O, Bensahel D, Faini G and Sagnes I 2000 *Appl. Phys. Lett.* **77** 1822
[166] Stoffel M, Denker U and Schmidt O G 2003 *Appl. Phys. Lett.* **82** 3236
[167] Alguno A, Usami N, Ujihara T, Fujiwara K, Sazaki G, Nakajima K and Shiraki Y 2003 *Appl. Phys. Lett.* **83** 1258
[168] Vescan L, Chretien O, Stoica T, Mateeva E and Muck A 2000 *Mater. Sci. Semicond. Process.* **3** 383

[169] Naval L, Jalali B, Gomelsky L and Liu J M 1996 *J. Lightwave Technol.* **14** 787
[170] Jalali B, Naval L and Levi A F J 1994 *J. Lightwave Technol.* **12** 1930
[171] ElKurdy M, Boucaud P, Sauvage S, Kermarrec O, Campidelli Y, Bensahel D, Saint-Girons G and Sagnes I 2002 *Appl. Phys. Lett.* **80** 509
[172] ElKurdi M, Boucaud P, Sauvage S, Fishman G, O, Kermarrec Y C, Bensahel D, Saint-Girons G, Patriarche G and Sagnes I 2003 *Physica* E **16** 523
[173] Tong S, Liu J L, Wan J and Wang K L 2002 *Appl. Phys. Lett.* **80** 1189
[174] Konle J, Presting H, Kibbel H, Thonke K and Sauer R 2001 *Solid-State Electron.* **45** 1921
[175] Winnerl S, Buca D, Lenk S, Buchal C, Mantl S and Xu D-X 2002 *Microelectron. Eng.* **64** 205
[176] Xu D-X, Janz S, Lafontaine H and Pearson M R T 1999 *Proc. SPIE Silicon-Based Optoelectronics* ed D C Houghton and E A Fitzgerald (San Jose, CA: SPIE) p 50
[177] El Kurdi M, Boucaud P, Sauvage S, Fishman G, Kermarrec O, Campidelli Y, Bensahel D, Saint-Girons G, Patriarche G and Sagnes I 2003 *Physica* E **16** 523
[178] Buca D, Winnerl S, Lenk S, Buchal C and Xu D-X 2002 *Appl. Phys. Lett.* **80** 4172
[179] Winnerl S, Buca D, Lenk S, Buchal C, Mantl S and Xu D-X 2002 *Mater. Sci. Eng.* B **89** 73
[180] Miesner C, Rothig O, Brunner K and Abstreiter G 2000 *Appl. Phys. Lett.* **76** 1027
[181] Miesner C, Brunner K and Abstreiter G 2001 *Infrared Phys. Technol.* **42** 461
[182] Sakamoto K, Matsuhata H, Tanner M O, Wang D and Wang K L 1998 *Thin Solid Films* **321** 55
[183] Liu F, Tersoff J and Lagally M G 1998 *Phys. Rev. Lett.* **80** 1268
[184] Zhu J-H, Brunner K and Abstreiter G 1998 *Appl. Phys. Lett.* **73** 620
[185] Xie Y H, Samavedam S B, Bulsara M, Langdo T A and Fitzgerald E A 1997 *Appl. Phys. Lett.* **71** 3567
[186] Teichert C, Hofer C, Lyutovich K, Bauer M and Kasper E 2000 *Thin Solid Films* **380** 25
[187] Leroy F, Eymery J, Gentile P and Fournel F 2002 *Appl. Phys. Lett.* **80** 3078
[188] Shiryaev S Y, Pedersen E V, Jensen F, Petersen J W, Hansen J L and Larsen A N 1997 *Thin Solid Films* **294** 311
[189] Voigtlander B and Theuerkauf N 2000 *Surf. Sci.* **461** L575
[190] Wang K L, Tong S and Kim H J 2005 *Mater. Sci. Semicond. Process.* **8** 389
[191] Perovic D D, Weatherly G C, Simpson P J, Schultz P J, Jackman T E, Aers G C, Noël J P and Houghton D C 1991 *Phys. Rev.* B **43** 14257–60
[192] Jackman T E, Aers G C, McCaffrey J P, Britton D, Willtzki P, Schultz P J, Simpson P J and Mascher P 1992 *Positron Annihilation: Proc. 9th Int. Conf. on Positron Annihilation (Zurich)* ed Z Kajcsos and C Szeles, p 301
[193] Baribeau J-M, Wu X, Lockwood D J, Tay L and Sproule G I 2004 *J. Vac. Sci. Technol.* B **22** 1479
[194] Baribeau J-M, Rowell N L, Wu X, Beaulieu M and Lockwood D J 2004 *Group-IV Semiconductor Nanostructures* ed L Tsybeskov, D J Lockwood, C Delerue and M Ichikawa (Pittsburgh, PA: Materials Research Society)
[195] Kamins T I and Williams R S 1997 *Appl. Phys. Lett.* **71** 1201
[196] Jin G, Liu J L, Thomas S G, Luo Y H, Wang K L and Nguyen B-Y 1999 *Appl. Phys. Lett.* **75** 2752
[197] Kamins T I, Ohlberg D A A, Williams R S, Zhang W and Chou S Y 1999 *Appl. Phys. Lett.* **74** 1773
[198] Kitajima T, Liu B and Leone S R 2002 *Appl. Phys. Lett.* **80** 497
[199] Zhong Z, Halilovic A, Muhlberger M, Schäffler F and Bauer G 2003 *J. Appl. Phys.* **93** 6258
[200] Zhong Z, Halilovic A, Muhlberger M, Schäffler F and Bauer G 2003 *Appl. Phys. Lett.* **82** 445
[201] Zhong Z, Halilovic A, Fromherz T, Schäffler F and Bauer G 2003 *Appl. Phys. Lett.* **82** 4779
[202] Zhong Z, Halilovic A, Lichtenberger H, Schäffler F and Bauer G 2004 *Physica* E **23** 243
[203] Kukta R V and Kouris D 2005 *J. Appl. Phys.* **97** 033527
[204] Schmidt O G, Lange C, Eberl K, Kienzle O and Ernst F 1997 *Appl. Phys. Lett.* **71** 2340
[205] Schmidt O G, Schieker S, Eberl K, Kienzle O and Ernst F 1998 *Appl. Phys. Lett.* **73** 59
[206] Schmidt O G, Lange C, Eberl K, Kienzle O and Ernst F 1998 *Thin Solid Films* **336** 248
[207] Dentel D, Vescan L, Chrétien O and Holländer B 2000 *J. Appl. Phys.* **88** 5113
[208] Wakayama Y, Sokolov L V, Zakharov N, Werner P and Gosele U 2003 *Appl. Surf. Sci.* **216** 419
[209] Baribeau J-M, Lockwood D J, Balle J, Rolfe S J and Sproule G I 2002 *Mater. Sci. Eng.* B **89** 296
[210] Baribeau J-M, Lockwood D J, Balle J, Rolfe S J, Sproule G I and Moisa S 2002 *Thin Solid Films* **410** 61
[211] Shao X *et al* 1999 *J. Appl. Phys.* **85** 578
[212] Dentel D, Bischoff J L, Kubler L, Stoffel M and Castelein G 2003 *J. Appl. Phys.* **93** 5069
[213] Leifeld O, Beyer A, Muller E, Grützmacher D and Kern K 2000 *Thin Solid Films* **380** 176
[214] Wakayama Y, Gerth G, Werner P, Gosele U and Sokolov L V 2000 *Appl. Phys. Lett.* **77** 2328
[215] Beyer A, Leifeld O, Muller E, Stutz S, Sigg H and Grützmacher D 2000 *Thin Solid Films* **380** 246
[216] Schmidt O G, Lange C, Eberl K, Kienzle O and Ernst F 1998 *Thin Solid Films* **321** 70
[217] Stoffel M, Simon L, Bischoff J L, Aubel D, Kubler L and Castelein G 2000 *Thin Solid Films* **380** 32

[218] Eberl K, Schmidt O G, Kienzle O and Ernst F 2000 *Thin Solid Films* **373** 164
[219] Sakai A and Tatsumi T 1994 *Appl. Phys. Lett.* **64** 52
[220] Baribeau J-M, Lockwood D J, Syme R W G and Labbé H J 1997 *Control of Semiconductor Surfaces and Interfaces* ed S M Prokes, O J Glembocki, S K Brierley, J M Gibson and J M Woodall (Pittsburgh, PA: Materials Research Society) p 113
[221] Portavoce A, Ronda A and Berbezier I 2002 *Mater. Sci. Eng.* B **89** 205
[222] Portavoce A, Volpi F, Ronda A, Gas P and Berbezier I 2000 *Thin Solid Films* **380** 164
[223] Eaglesham D J, Unterwald F C and Jacobson D C 1993 *Phys. Rev. Lett.* **70** 966
[224] Kamins T I, Medeiros-Ribeiro G, Ohlberg D A A and Williams R S 2004 *J. Appl. Phys.* **95** 1562
[225] Shi W H, Li C B, Luo L P, Cheng B W and Wang Q M 2005 *J. Cryst. Growth* **279** 329
[226] Brunner K and Zrenner A 2004 *Semiconductor Nanocrystals From Basic Principle to Applications* ed A L Efros, D J Lockwood and L Tsybeskov (New York: Kluwer–Academic/Plenum) p 112
[227] Wang K L, Liu J L and Jin G 2002 *J. Cryst. Growth* **237–239** 1892
[228] Yin H, Huang R, Hobart K D, Liang J, Suo Z, Shieh S R, Duffy T S, Kub F J and Sturm J C 2003 *J. Appl. Phys.* **94** 6875
[229] Yin H, Huang R, Hobart K D, Suo Z, Kuan T S, Inoki C K, Shieh S R, Duffy T S, Kub F J and Sturm J C 2002 *J. Appl. Phys.* **91** 9716
[230] Li C B, Cheng B W, Mao R W, Zuo Y H, Shi W H, Huang C J, Luo L P, Yu J Z and Wang Q M 2004 *Thin Solid Films* **467** 197